J. Fluid Mech. (2011), vol. 666, pp. 573–604. © Cambridge University Press 2011
doi:10.1017/S0022112010004544

Interactions within the turbulent boundary layer at high Reynolds number

M. GUALA[1]†, M. METZGER[2] AND B. J. McKEON[1]

[1]Graduate Aerospace Laboratories, California Institute of Technology, Pasadena, CA 91125, USA
[2]Department of Mechanical Engineering, University of Utah, Salt Lake City, UT 84112, USA

(Received 8 December 2009; revised 25 August 2010; accepted 25 August 2010)

Simultaneous streamwise velocity measurements across the vertical direction obtained in the atmospheric surface layer ($Re_\tau \simeq 5 \times 10^5$) under near thermally neutral conditions are used to outline and quantify interactions between the scales of turbulence, from the very-large-scale motions to the dissipative scales. Results from conditioned spectra, joint probability density functions and conditional averages show that the signature of very-large-scale oscillations can be found across the whole wall region and that these scales interact with the near-wall turbulence from the energy-containing eddies to the dissipative scales, most strongly in a layer close to the wall, $z^+ \lesssim 10^3$. The scale separation achievable in the atmospheric surface layer appears to be a key difference from the low-Reynolds-number picture, in which structures attached to the wall are known to extend through the full wall-normal extent of the boundary layer. A phenomenological picture of very-large-scale motions coexisting and interacting with structures from the hairpin paradigm is provided here for the high-Reynolds-number case. In particular, it is inferred that the hairpin-packet conceptual model may not be exhaustively representative of the whole wall region, but only of a near-wall layer of $z^+ = O(10^3)$, where scale interactions are mostly confined.

Key words: atmospheric flows, turbulent boundary layers, turbulent flows

1. Introduction

Over the last few years, the boundary-layer turbulence community has seen a major reinterpretation of Townsend's self-similarity principle thanks to a series of numerical and experimental investigations that have explored the significance of the very-large-scale motions (VLSMs), most commonly observed as the statistical signature of coherence in the streamwise velocity over six to ten boundary-layer thicknesses, δ; see for example del Álamo & Jiménez (2003), Guala, Hommema & Adrian (2006), Balakumar & Adrian (2007), Monty *et al.* (2007) and Marusic & Hutchins (2008). In particular, the definition of 'active' and 'inactive' motions in the sense of Townsend has been revisited, alongside a renewed investigation of the Reynolds number dependency of the near-wall velocity field (e.g. Metzger & Klewicki 2001; Morrison *et al.* 2004; Hutchins & Marusic 2007*a*; Morrison 2007; Mathis, Hutchins & Marusic 2009), which has been extended to a predictive model for

† Email address for correspondence: guala@caltech.edu

the near-wall peak given limited off-wall information (Marusic, Mathis & Hutchins 2010). A major result arising from the former set of contributions is that VLSMs, also referred to as super-delta scale motions, superstructures or stripes, carry a considerable portion of turbulent kinetic energy and Reynolds stress, and influence the near-wall turbulence through an amplitude modulation-like process. These structures have been known to exist for several decades (see e.g. Favre, Gaviglio & Dumas 1967; Kovasznay, Kibens & Blackwelder 1970), but there had been relatively few quantitative studies on their statistical and energetic relevance until the paper of Kim & Adrian (1999), as compared to the studies devoted to near-wall turbulent coherent structures such as hairpins, horse cane vortices and longitudinal streaks. While the latter structures have been well documented and some theoretical and conceptual arguments have been provided to link near-wall streaks with hairpin-like vortices and hairpin packets (Adrian, Meinhart & Tomkins 2000; Waleffe 2001; Adrian 2007), the formation, evolution and characteristics of the VLSMs still deserve further research.

It is inferred from several papers of Adrian and co-authors (Kim & Adrian 1999; Adrian *et al.* 2000; Christensen & Adrian 2001; Tomkins & Adrian 2003; Balakumar & Adrian 2007) that the hairpin vortex can be considered to be statistically representative of the (often asymmetric) structure near the wall, that hairpin vortices align into packets and that hairpin packets tend to align in the streamwise and spanwise directions. This alignment was hypothesized to lead to the formation of low-velocity coherent regions or 'bulges', which consist of several hairpin packets and thus extend to several boundary layer thicknesses in the flow direction and up to the boundary layer height or equivalent outer length scale. This effective confinement between the wall and the outer edge of the boundary layer constrains single hairpins embedded in a packet to potentially limited growth in the wall-normal direction with an additional degree of freedom in the spanwise direction. In these laboratory studies, most of the interplay in the wall-normal direction has been shown to occur between the near-wall streaks and hairpin self-organization mechanisms, as proposed by Waleffe (2001), while the development of bulges, a potential mechanism for the evolution of VLSM, was shown to occur mostly in the log and outer layer in both the streamwise and spanwise directions (Adrian *et al.* 2000; Tomkins & Adrian 2003). Most of these investigations, however, were based on laboratory scale experiments, with friction Reynolds number limited to several thousands. In such flows, there is no clear spectral separation between large-scale motions and the near-wall turbulence (see e.g. del Álamo & Jiménez 2003; McKeon & Sreenivasan 2007; Hutchins & Marusic 2007*b*).

When the Reynolds number increases, the above picture becomes more complex since near-wall streaks, large-scale coherent structures such as hairpins and hairpin packets, and VLSMs coexist, interact and likely 'originate' in different regions of the wall layer. For instance, the increasing amplitude of the near-wall peak of the streamwise velocity fluctuations u'/u_τ at $z^+ \sim 20$ (where $z^+ = zu_\tau/\nu$ is the wall-normal distance normalized with the viscous scale, namely the ratio of the kinematic viscosity ν and the friction velocity $u_\tau = \sqrt{\tau_w/\rho}$, where τ_w is the wall shear stress and ρ is the fluid density) with increasing friction Reynolds number $Re_\tau = \delta u_\tau/\nu$ (δ is the boundary layer thickness) in turbulent boundary layers can be interpreted as the result of the interaction between motion on a scale that is not described by inner scaling and the near-wall, inner-scaling turbulence. This, however, is a statistical argument for a structural interaction. More quantitative work is needed in order to substantiate such a claim.

Here lies the motivation of our work: to identify and characterize the structural features of the high-Reynolds-number turbulent boundary layer and to quantify the possible scale interactions across the wall layer. In order to interpret and quantify the large-scale–near-wall turbulent interaction, we should first understand where, statistically, the various structures that are known to populate the turbulent boundary layer flows at moderate Reynolds number lie in high-Reynolds-number boundary layers. We stress that a clear separation between scales implies a thick inertial range in both physical and spectral domains and a likely lack of an upper constraint felt by evolving vortical structures.

According to the literature based on results at moderate and high Reynolds numbers, it appears that near-wall streaks develop in the region immediately close to the wall and are well-described by inner-scaling arguments. Larger scale structures such as hairpins and hairpin packets likely reach further from the wall, at least into the overlap region. The attached eddy model of Perry & Chong (1982) proposes a hierarchy of structures that scale on distance from the wall. It is an open question up to which height organized coherent motions can be interpreted in the framework of the hairpin-packet conceptual model, or more simply put, how far from the wall single hairpins can grow. Though we cannot exhaustively answer all these questions, we pose them for the sake of clarity and as a topic of future research.

It is clear that questions of scale interaction must be studied in a frame of reference with sufficient scale separation to permit unambiguous definitions of inner and outer scales and subsequent classification of wall turbulent structures. The atmospheric surface layer is seen as a useful benchmark for such experiments (see e.g. Metzger & Klewicki 2001; Gulitski *et al.* 2007 and references therein) because it represents a sole truly high-Reynolds-number facility. The challenges associated with field tests in this environment are significant and will be detailed below.

In the next section, the experimental apparatus is summarized with an emphasis on the limitations of the measuring set-up. Section 3 is devoted to the presentation of the major turbulent statistics focusing on the representativeness of our results in the context of canonical high-Reynolds-number zero-pressure-gradient turbulent boundary layers. Two-dimensional spectral analysis is then presented to introduce a quantitative method to analyse scale separation, and two filtering options are provided in order to divide the large-scale motion from the smaller scales of turbulence. The core of the scale interaction analysis is presented in §4, where the effects are quantified in both probabilistic and spectral terms. In §5 we attempt a phenomenological interpretation of our statistical results. Concluding remarks follow.

2. Experimental considerations

Despite limited control of the free-stream velocity, surface roughness and boundary layer thickness on the one hand and stratification or buoyancy instability effects on the other, selected measurements in the atmospheric surface layer (ASL) under thermally neutral conditions can provide a reliable picture (or at worst scaling trends) of the turbulent boundary layer at high Reynolds number with limited drawbacks arising from positioning error and/or finite sensor size (Metzger, McKeon & Holmes 2007). As a result of this, in conditions with stable wind direction and magnitude and with continuously monitored heat and momentum fluxes, measurements in the ASL can be a benchmark for flows with friction Reynolds number $Re_\tau = \delta u_\tau/\nu \simeq 5 \times 10^5$.

Experiments were conducted in the ASL under very near thermally neutral (henceforth 'near neutral') conditions during a two-week field campaign at the

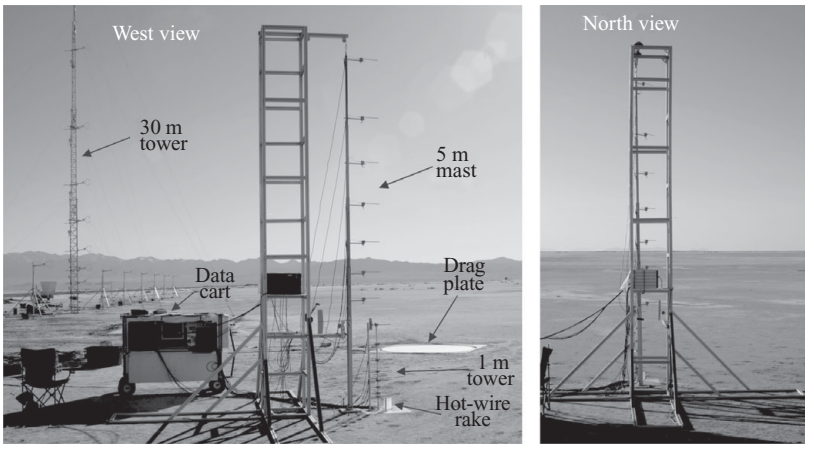

FIGURE 1. Experimental set-up, showing the hot-wire array in the foreground with the 30 m tower and sonic anemometers in the background.

University of Utah Surface Layer Turbulence and Environmental Science Test (SLTEST) facility located on the southern end of the salt flats of the Great Salt Lake Desert. The desert consists of a silty-clay playa, devoid of vegetation and extremely flat. Sparse crust imperfections constituting the actual surface roughness yield an aerodynamic roughness length, z_0, in the range $0.2 \leqslant z_0 \leqslant 0.5$ mm, defined such that $\kappa\, U(z)/u_\tau = \log(z/z_0)$, where κ is the von Kármán constant. The variation of water content in proximity to the surface controls the surface roughness during the course of the year. The relatively wet playa in spring is smoother than the drier conditions observed later in summer, when small cracks are formed on the surface, leading to values of aerodynamic roughness length z_0 or equivalent sand roughness k_s which may vary between campaigns depending on the respective dates and durations.

The measuring set-up (figure 1) consisted of 31 single hot-wire probes logarithmically spaced in the vertical direction and sampled at 5 kHz to provide simultaneous records of the streamwise velocity over the first 5 m of the surface layer, and a nearby, but non-co-located 30 m tower with nine sonic anemometers providing simultaneous acquisition of the three velocity components and temperature at 20 Hz. More details about the experimental apparatus, measuring technique and data validation can be found in Metzger *et al.* (2007). Here we briefly provide the key information. We use the notation $\hat{U}(z,t) = U(z) + u(z,t)$, etc., such that U denotes the mean horizontal wind speed at wall-normal height z. Since the measurement domain did not span the boundary layer thickness, the mean velocity value at the highest vertical location $U(z_{max})$ is used, where necessary, as a normalizing outer velocity scale.

The hot-wire array consisted of 15 wires on a surface-mounted rake, eight on a 1 m tower and a further eight on a second, 5 m tall tower. The wires were spaced over a distance 1 mm $\leqslant z \leqslant$ 4.6 m, i.e. in or below the logarithmic overlap region for a boundary layer height of 50–100 m, and were fabricated from 5 μm diameter tungsten wire, copper plated at the ends with a 1 mm active (unplated) region in the centre. Thus, $l^+ < 10$ in all cases, i.e. the non-dimensional wire length was always less than 10 viscous units and there are no probe resolution concerns. Calibrations of all of the hot wires were performed prior to and following each experiment. The length of the individual data records was 210 s, limited primarily by stationarity considerations and

the data acquisition system. Between runs the hot-wire rake and tower were rotated into the mean wind direction, as determined by visually inspecting a cup and vane anemometer at $z = 1$ m.

The stability parameter z/L, where L is the Monin–Obukhov length scale, was computed as a function of time of the day from sonic anemometers at four different heights ($1.4 \leqslant z \leqslant 12.5$ m). The measurements presented here were obtained in time periods over which $|z/L| \leqslant 0.01$ for the sonic anemometer located at $z = 1.4$ m and, thus, provide a very good estimate of near-neutral conditions (Mahrt 1998). Near-thermal neutrality, as defined by the strict condition $|z/L| \leqslant 0.01$ at all sonic anemometer locations, was observed to occur only for periods of the order of 10 min each evening transition throughout the field campaign. By enforcing this strict condition, our record lengths are necessarily relatively short, the effect of which will be discussed extensively in the following section.

In the present study, the friction velocity was derived from sonic anemometer measurements at $z = 1.4$ m such that $u_\tau \approx \langle uw \rangle^{1/2} = 0.14\ \mathrm{m\,s^{-1}}$, where u and w are the streamwise and wall-normal velocity fluctuations, respectively, and the angle brackets denote averaging over a suitable period in the sonic anemometer data. The estimated equivalent sandgrain roughness height, $k_s^+ = 50$, suggests that the selected runs are in the transitionally rough regime, implying that results for $z^+ = 3k_s^+ < 150$ (see Flack, Schultz & Shapiro 2005) must be considered to lie within the roughness sublayer. The height of the surface layer $\delta_{SL} = 50$ m was inferred from a set of previous measurements at the same location under similar stability conditions (see Metzger *et al.* 2007).

2.1. *Statistical convergence*

The spectral gap, defined as the intermediate frequency band in the one-dimensional power spectra of the velocity that provides essentially zero contribution to the turbulent kinetic energy, was obtained from the sonic anemometer at $z = 1.4$ m during the near-neutral period. The corresponding averaging time was estimated as $\tau_c = 3.30$ min, which is very close to our continuous recording samples (210 s).

The limited time period of each run corresponds to a VLSM turnover time of approximately 15–20 $TU(z_{max})/\delta$ (where $U(z_{max})$ is the mean velocity at the highest vertical measurement location). According to the criteria provided by Guala *et al.* (2006) and Balakumar & Adrian (2007) for the spectral classification of VLSM, the acquisition time should be large enough to capture most of the scales contributing to the VLSM (larger than $2\pi\delta$). While Hutchins & Marusic (2007) have proposed that the extent of superstructures can exceed $20\,\delta$ in the streamwise direction, it should be noted that such observations are based on measurements in a wall-parallel plane, such that extended coherence associated with spanwise meandering can be captured. The peak VLSM energy captured by point measurements, as in these experiments, is known to occur for wavelengths close to $2\pi\delta$. Therefore, while a single run cannot lead to a smooth spectrum and fully converged statistics, it can be expected to capture at least one complete oscillation of a VLSM. However, according to the cumulative plots shown in Balakumar & Adrian (2007), a turnover time of $TU(z_{max})/\delta = 20$ should account for only 80 %–90 % of the Reynolds stress contribution (note that such an estimate may suffer from Reynolds number effects). While longer acquisition periods would be desirable, they would come at the expense of a loss of precision in thermal conditions, wind direction and magnitude, and hence non-dimensional probe position. We stress that though the finite temporal duration of the runs represents a problem in terms of statistical convergence of high-order moments, it does minimize

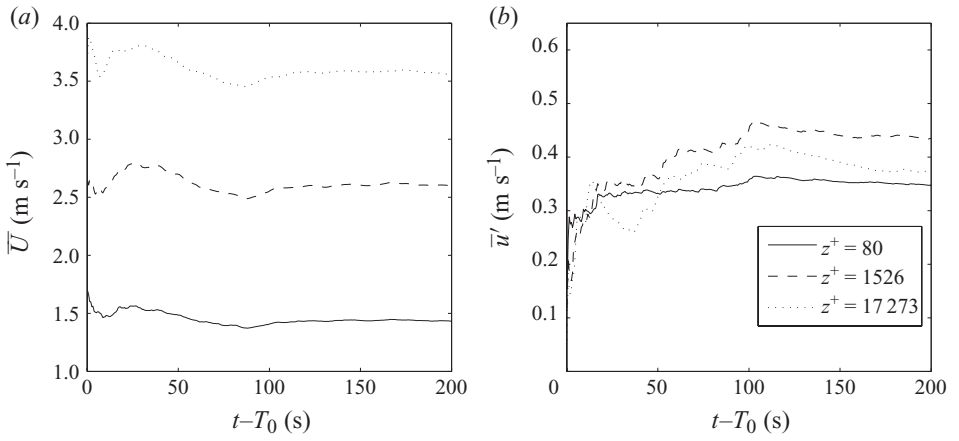

FIGURE 2. The effect of the averaging time $t - T_0$ on (a) mean and (b) r.m.s. fluctuating velocities at wall-normal locations in the range $z/\delta \sim 1 \times 10^{-4}$ to 3×10^{-2}.

unsteadiness and non-stationarity effects. This ensures that the boundary conditions at the wall and at the upper boundary, the friction velocity u_τ and $U(z_{max})$ respectively, remain relatively constant, implying that both the normalization in inner-wall units is extremely reliable (there is no variation of z^+ due to drift in u_τ) and the estimate of the local stability parameter is robust (again, no effects from a varying u_τ or $|z/L|$, in contrast to studies that achieve better convergence through longer sample times). As a result, any future comparisons between this study and results obtained in controlled laboratory scale flows or by numerical simulations could be considered to be relatively rigorous.

Obtaining statistical convergence during the near-neutral period in the surface layer is always a challenge. Considerable effort was devoted to quantifying the statistical issues associated with our relatively short sample times. Unsteadiness effects, typically discussed in the context of field measurements in the surface layer, do not seem to be relevant. The variation of the mean and root-mean-square (r.m.s.) fluctuating velocities with a varying averaging time is shown in figure 2. Specifically, for each time t we plot the mean and fluctuating (r.m.s.) velocities, denoted by $\overline{U}$ and $\overline{u'}$ respectively, computed over a (averaging) time interval equal to $t - T_0$ (where T_0 is the initial time of the measurement). Despite a few weak oscillations, especially farther from the wall ($z^+ > 10^4$), the statistical convergence is reasonable.

The limited temporal extent of our data also has implications on the robustness of the statistical results provided in this paper, in particular for cross- and auto-correlations. The window size for these computations must be carefully chosen in order to properly resolve the large scales. In figure 3, the effect of window size, T_{max}, on the computed value of the integral scale, T_{int}, is shown. The latter is obtained as the integral of the autocorrelation function and compared with two other representative time scales $T_{0.2}$, $T_{0.5}$, related to the values of the normalized autocorrelation function of 0.2 and 0.5, respectively. We note that the estimate of the integral scale varies with T_{max}, i.e. with the maximum resolved time scale, for short averaging times. However, for $T \simeq 25$ s, the quantities T_{int}, $T_{0.2}$, $T_{0.5}$ reach a plateau. For large T_{max}, we observe some significant oscillations in the tail of the autocorrelation function, particularly far from the wall, such that the scale $T_{0.2}$ is consistently more affected than the other scales (a consequence of the sample lengths). The value of $T_{max} = 26$ s is then chosen for the estimation of correlation functions. This is a compromise between the choice

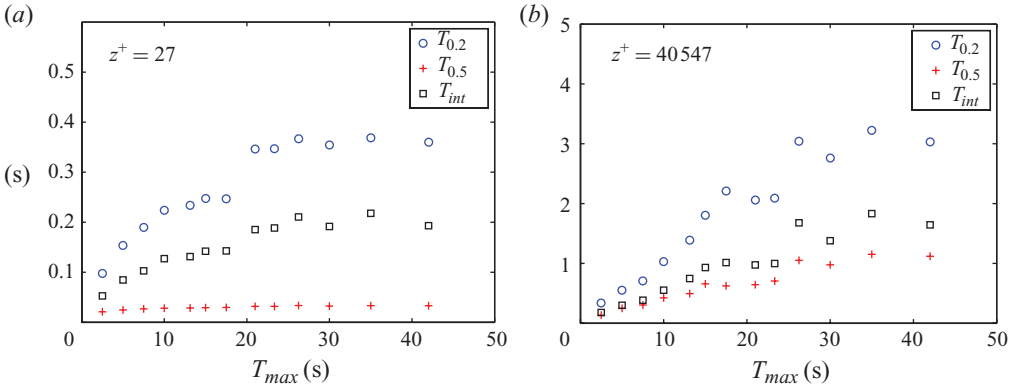

FIGURE 3. (Colour online) (a, b) The effect of the averaging time T_{max} on the integral time scale, T_{int}, $T_{0.2}$ and $T_{0.5}$ presented in seconds.

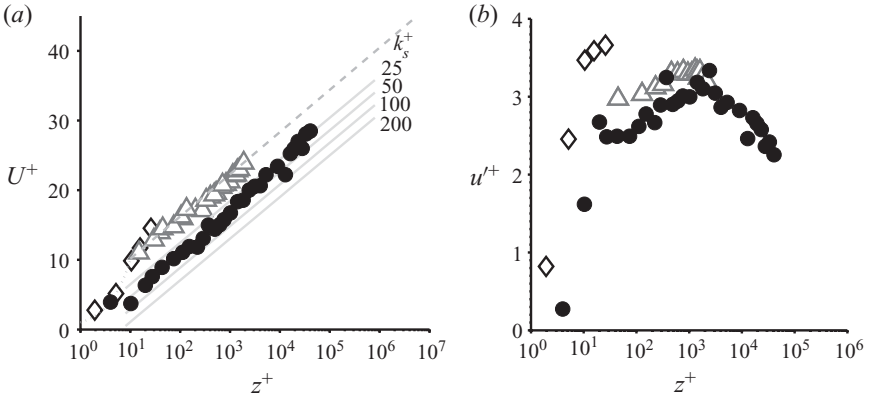

FIGURE 4. (a) Mean and (b) r.m.s. velocity profiles, plotted in dimensionless inner units and compared with other results from the near-neutral atmospheric surface layer. Symbols: ●, present data; △, Metzger & Klewicki (2001); ◇, hot-wire rake (2002 data, see Metzger *et al.* 2007).

of a larger time window, leading to fewer correlation functions calculated for each run and less smoothing associated with the ensemble average, or a smaller time window in which the ensemble-averaging procedure reduces the noise but T_{max} is too small to resolve the large scales. In addition, we can argue that the integral time scales T_{int}, $T_{0.2}$, $T_{0.5}$ seem to reach an acceptable plateau for $T_{max} > 26$ (figure 3*a*, *b*).

3. Velocity statistics

Mean and fluctuating velocity statistics, as well as auto-correlations and two-point correlation functions, are presented and discussed in the following in the context of a canonical zero-pressure-gradient high-Reynolds-number turbulent boundary layer, with reference to the experimental constraints described above.

3.1. *Mean and fluctuating velocities*

The mean and r.m.s. streamwise velocity profiles are shown in figures 4(*a*) and 4(*b*), respectively. The value of $u_\tau = 0.14\ \mathrm{m\,s^{-1}}$ provided by the sonic anemometers is in reasonable agreement with the fitting of the mean velocity profile U (figure 4*a*)

and both profiles agree well with previous measurements obtained in near-neutral atmospheric flows. Approximate locations of the log law with $\kappa = 0.39$ and the Hama roughness function for various roughness heights are marked for reference. The mean profile suggests an equivalent sandgrain roughness for the current measurements of $k_s^+ = 50$, an estimate that is supported by a reduced near-wall peak in r.m.s. velocity compared with smoother wall results from previous campaigns.

As discussed above, the surface roughness is highly dependent on the time of year and playa condition, leading to estimates of aerodynamic roughness length z_0 or equivalent sand roughness k_s, which can vary essentially between the smooth and transitionally rough regimes for different sets of experiments (Metzger & Holmes 2008). For instance, near-wall hot-wire measurements by Metzger in 2003 (included in Metzger *et al.* 2007) are characterized by k_s^+ as high as 50, while sonic anemometer measurements further from the wall (e.g. Hutchins & Marusic 2007) were considered to indicate a hydrodynamically smooth wall. It is however noteworthy that the aerodynamic roughness length can be estimated accurately only when either the mean velocity profile is well resolved in the wall-normal direction, allowing for a robust fit of the logarithmic law of the wall, or the friction velocity is known with some confidence.

Regarding the current dataset, our estimate of $k_s^+ = 50$ implies that results within at least three equivalent sandgrain roughness heights, $z^+ < 3k_s^+ = 150$, must be interpreted with roughness effects in mind (see Flack *et al.* 2005). A transitionally rough wall can be considered to introduce a contamination of the near-wall turbulence due to small-scale vorticity shed by the protrusion of roughness elements (mostly sand grains or surface alteration) from the viscous sublayer. Such a mechanism is known to damp the near-wall streamwise velocity fluctuations by partially disrupting the organization of near-wall streaks while favouring the development of wall-normal velocity fluctuations (see e.g. Ikeda & Durbin 2007; Orlandi & Leonardi 2008), with concurrent results of reduced anisotropy and a possible shortening of streamwise length scales close to the wall.

However, we have several indications that our experimental results for $z^+ > 150$ are statistically comparable with results obtained in the smooth regime. The shear rate parameter, $S* = Sq^2/\epsilon$, where the vertical derivative of the mean velocity $S = \partial U/\partial z$, $q = (\langle u'^2 + v'^2 + w'^2 \rangle)^{0.5}$ and ϵ is the energy dissipation, was investigated following the analysis of Lee, Kim & Moin (1990). Approximating q using only the streamwise velocity component, $q = (\langle u'^2 \rangle)^{0.5}$, $S* = Sq^2/\epsilon > 6$ in a layer $z^+ < 4000$, indicating strong anisotropic effects and suggesting a streak-like type of turbulence, typical of the smooth wall regime. In addition, the exponents of the streamwise velocity structure functions were estimated up to order 6 and found to be in agreement with the values in the literature obtained in smooth-wall wind-tunnel studies. Significant multiscaling behaviour, typically associated with near-wall anisotropy, was consistently observed at $z^+ < O(10^3)$ (see Guala, Metzger & McKeon 2010 and references therein). As shown in the following sections, the structure inclination angle representative of dominant ramp-like aggregation is also in agreement with typical values in smooth wall turbulence, as compared with larger values observed on rough surfaces (e.g. Krogstad, Kaspersen & Rimestad 1998). Thus, we will interpret our results in the context of smooth walls for all but the nearest points to the wall.

3.2. *Autocorrelation, integral scales and two-point correlation functions*

Full autocorrelation functions at two wall-normal locations are presented in figure 5. The derived integral time scales and alternative time scales $T_{0.2}$ and $T_{0.5}$

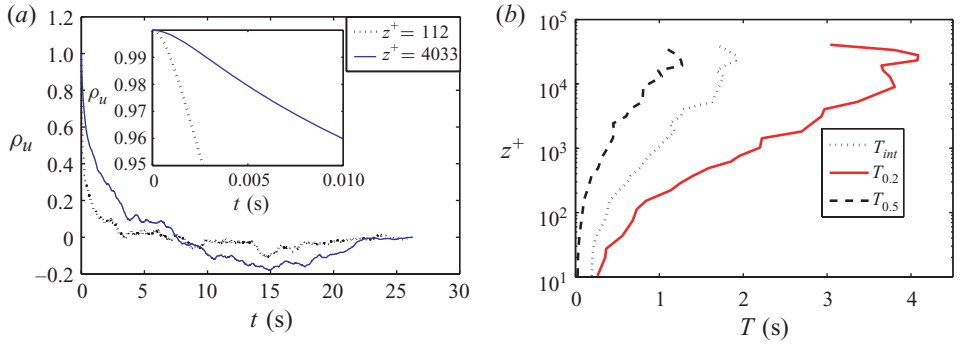

FIGURE 5. (Colour online) (*a*) Autocorrelation functions $\rho_u(t)$ at $z^+_{ref} = 112$ and $z^+_{ref} = 4032$. (*b*) Comparison of the wall-normal variation of the integral scale T_{int} with $T_{0.2}$ and $T_{0.5}$, respectively, associated with $\rho_u = 0.2$ and $\rho_u = 0.5$.

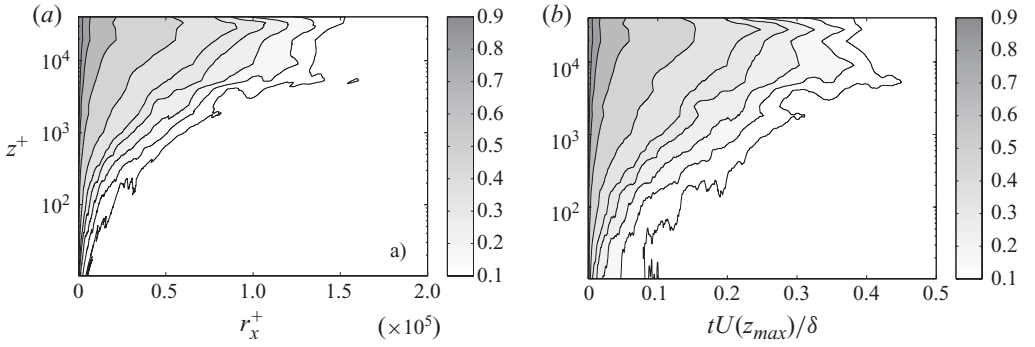

FIGURE 6. Wall-normal variation of contours of the autocorrelation function ρ_u in the (*a*) spatial and (*b*) temporal domains.

are also provided as a function of z^+. Figure 6 shows the wall-normal variation of the autocorrelation in both temporal and spatial domains, where Taylor's hypothesis of frozen turbulence has been used for the conversion between domains such that the spatial lag r_x^+ is obtained by multiplying the time lag by the mean velocity value at each z^+. Both the autocorrelation functions and the estimated integral time scales are well resolved across the whole wall layer using the averaging time of 26 s discussed in the previous section. We apply the same averaging window to the calculation of the two-point correlation functions, which is known to reflect the statistical imprint of the coherent structures populating the wall region.

Assuming spatial homogeneity in the streamwise direction, the two-point spatial correlation coefficient of the streamwise fluctuating component of the velocity is given by

$$\rho_{uu}\left(r_x^+, z^+, z^+_{ref}\right) = \frac{\sum_x u(x, z_{ref})u(x + r_x, z)}{u'(z_{ref})u'(z)}. \tag{3.1}$$

Figures 7 and 8 show isocontours of the two-point spatial correlation coefficient with reference heights close to the wall and well into the overlap region, $z^+_{ref} = 120$ and $z^+_{ref} = 4032$. A line inclined at 11° to the wall is added to both plots for reference. When z^+_{ref} is close to the wall, the typical elongated and inclined correlation shape

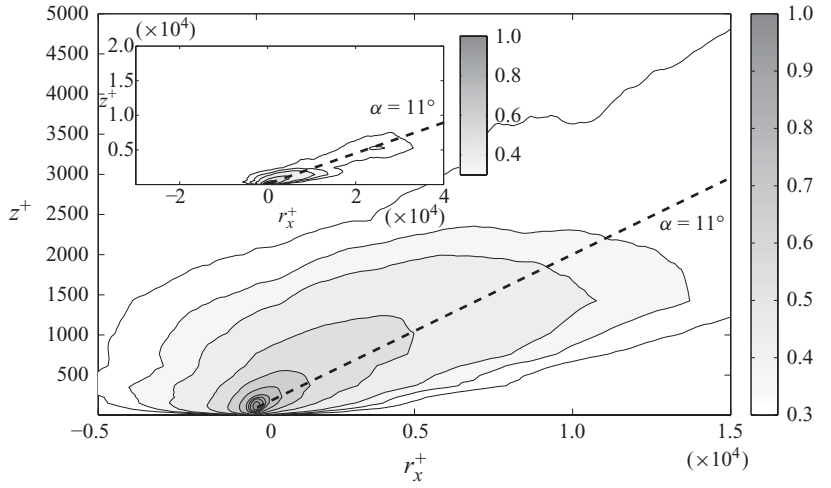

FIGURE 7. Isocontours of the two-point correlation function $\rho_{uu}(r_x^+, z^+, z_{ref}^+)$ at $z_{ref}^+ = 120$. The same contours are plotted in the inset to compare with ρ_{uu} at $z_{ref}^+ = 4032$ plotted in figure 8.

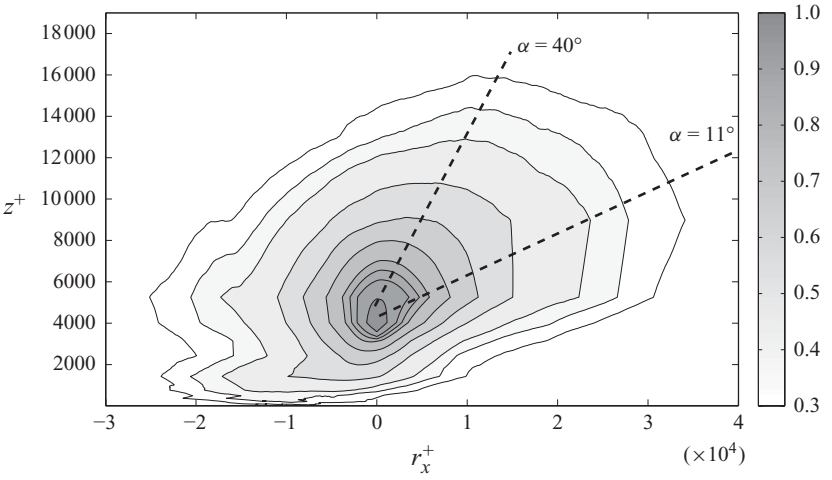

FIGURE 8. Isocontours of the two-point correlation function $\rho_{uu}(r_x^+, z^+, z_{ref}^+)$ at $z_{ref}^+ = 4032$.

(e.g. Christensen & Adrian 2001 and references therein) is observed, but there is a significant change in the shape of the two-point correlation contour as the wall-normal distance z_{ref}^+ is increased. For larger z_{ref}^+, the contours exhibit a fuller shape, while still retaining the imprint of the elongated tail that resembles the near-wall shape for $z < z_{ref}$. In particular, close to the wall the ρ_{uu} contour has the typical shape that has been associated with a hairpin-packet structure (Adrian *et al.* 2000), while further from the wall the shape changes, indicating coherence more localized in x and z. While the vertical resolution is coarse, especially for large z^+, and interpolation is used between the probe locations, the temporal resolution is very fine. In the inset of figure 7, we show the two-point correlation contours in a domain comparable with figure 8. The signature of ramp-like structures, following the characteristic angle, seems to extend in the inset of figure 7 up to $z^+ = 10^4$. However, with $z_{ref}^+ \sim 10^3$, the signature of ramp-like aggregation appears strongly contaminated (see figure 8).

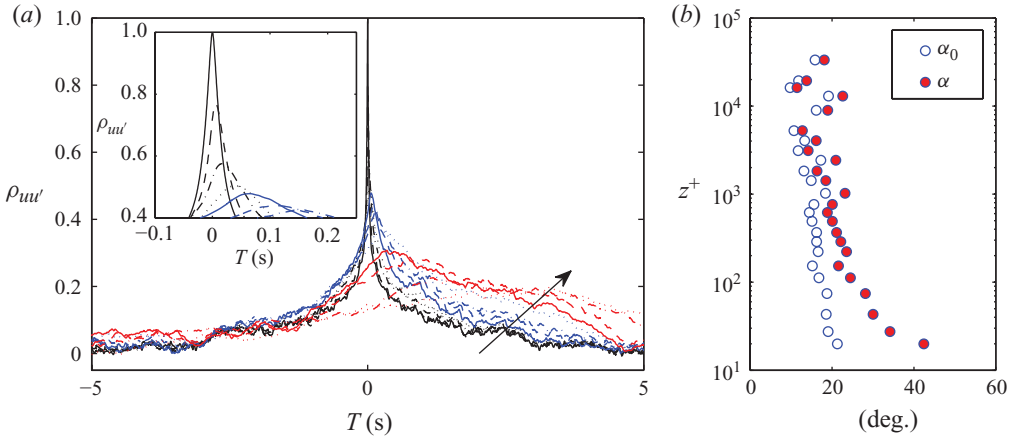

FIGURE 9. (Colour online) (*a*) Cross-correlation functions $\rho(u, u')$ between $u(t, z^+ = 10)$ and $u'(t, z^+)$ at 12 different heights in the range $10 < z^+ < 616$ (increasing z^+ in the direction of the arrow). (*b*) Profile of the inclination angle imposing null mean velocity close to the wall (α_0), or using the finite velocity at the wall (α).

Given the uncertainty associated with the 'frozen turbulence' hypothesis at very large scales, which are probably not 'frozen', the use of a single convective velocity independent of z^+ to convert between time and space was also considered. The qualitative shapes of the two contour plots do not change. However, the typical inclined two-point correlation contours of figure 7 become flatter or steeper due to the relative stretching or compression of spatial scales at increasing distance from the wall, depending on the choice of constant velocity. Regardless of any reasonable choice for the advective velocity used in the frozen turbulence assumption, we observe a qualitatively different shape while comparing ρ_{uu} at $z^+_{ref} = 112$ and $z^+_{ref} = 4032$.

In terms of z^+ there is a significant difference between the z^+_{ref} values, more than an order of magnitude; however, in the ASL this entire region resides in or below the overlap region, i.e. $z/\delta = 2.7 \times 10^{-4}$ to 1×10^{-2}. The regime represented by figure 8 is simply not accessible in most wind-tunnel studies, but the onset of a similar structure can be observed in the correlation measurements of Tutkun *et al.* (2009) at $Re_\tau \simeq 1.0$–1.9×10^4. However, while the shape of the two-point correlation at such moderate Re_τ is observed to change mostly between the inner and the outer layers, at the high Reynolds number investigated here we observe a strong change still within the log layer. Similar features are also observed in the conditional averages in the channel flow at $Re_\tau = 2 \times 10^5$ of Chung & McKeon (2010), suggesting that this is a legitimate feature of truly high-Reynolds-number wall turbulence rather than an artefact of other processes at work in the ASL. The implication is that further from the wall, the streamwise velocity exhibits even longer coherence with a reduced wall-normal variation in the spatial phase.

The typical angle of inclination of wall structures, α, can be estimated directly by converting the time delay in the cross-correlation function between the local velocity and the velocity at the wall to a spatial distance. Figure 9 shows the cross-correlations and the resultant variation of α with wall-normal distance. An accurate estimate of this angle requires a velocity signal very close to the wall or a direct measure of the shear stress (see Marusic & Heuer 2007); however, our closest measurement to the wall is at $z^+ \sim 10$ and corresponds to a non-negligible mean velocity. A

better estimate of the angle, denoted by α_0, can be obtained by assuming zero mean velocity at the wall, i.e. by calculating the spatial lag as $\delta x(z) = U(z)\delta t$. The values of α_0 reported in figure 9 are more consistent with the 10°–20° angles reported in the literature and confirm the findings of Marusic & Heuer (2007) that the angle of inclination in the surface layer is substantially invariant, in good agreement with lower-Reynolds-number results, and very sensitive to the reference location. A local maximum of the cross-correlation in the region of this angle can be distinguished up to $z^+ \sim 4 \times 10^4$.

4. Interactions across the wall layer

4.1. *A visual inspection of scale interactions*

The simultaneous nature of the measurements of the streamwise velocity component across the wall layer permits instantaneous visualization of long time-scale velocity oscillations that influence a considerable region of the wall layer. A sample full temporal and (interpolated) wall-normal domain of our selected measurements is shown in figure 10. Figure 10(*a*, *b*) shows the local mean velocity on both a logarithmic scale representative of the probe spacing and a linear scale. In this figure, the local mean and r.m.s. velocities are defined using a sliding window with averaging time $\tau = 1$ s, i.e.

$$\tilde{U}(z,t) = \frac{1}{\tau}\int_{t-\tau/2}^{t+\tau/2} \hat{U}(\tau, z)\mathrm{d}\tau, \quad \tilde{u}'(z,t) = \left[\frac{1}{\tau}\int_{t-\tau/2}^{t+\tau/2} (\hat{U}(\tau, z) - \tilde{U}(z,t))^2 \mathrm{d}\tau\right]^{1/2}, \qquad (4.1)$$

where $\tilde{\cdot}$ denotes the sliding window value of the variable. The averaging time is somewhat arbitrary, beyond being close to a time scale associated with the outer edge of the inner scaling, $\tau \approx 0.1\delta/U(z = 0.1\delta)$. However, the qualitative shapes of the contours do not change significantly with the averaging time.

A persistent oscillation of the local mean velocity $\tilde{U}$, with a period of roughly 60–80 s, characterizes the whole domain. Such an oscillation corresponds to about 6 times the boundary layer thickness in spatial terms and can thus be regarded as a VLSM. Although the VLSMs deserve an outer scale normalization, we do not have an accurate estimate for δ or the free-stream velocity; therefore, we maintain a dimensional form for the time axis for these plots. At $t = 90$–100 s, we can identify a large-scale event, seemingly 'sweeping' high-speed fluid towards the wall and affecting the local (sliding window) r.m.s. streamwise velocity $\tilde{u}'$, as shown in figure 10(*c*). We will show below that this measure of the r.m.s. reflects both large- and small-scale activities, indicating an interaction across scales. A comparison of a select few contours of the local mean velocity and the local r.m.s. velocity in figure 10(*d*) shows that at smaller time scales, the phase relationship between the variation of $\tilde{U}$ and $\tilde{u}'$ is more complex. It is proposed that these relationships can be studied quantitatively by conditional statistics, spectral analysis and probabilistic tools.

The interpretation of such large-scale structures, which possibly also include a spanwise 'meandering' component, still challenges the current view of large-scale motion, generally classified to date through spectral analysis in wavenumber space (see e.g. Guala *et al.* 2006; Balakumar & Adrian 2007; Hutchins & Marusic 2007*a*). Since these oscillations appear to affect the whole layer, the typical conversion between the frequency and wavenumber domains is not trivial. It is well known that large scales travel with a convective velocity which is generally higher than the mean velocity close to the wall (see Morrison, Bullock & Kronauer 1971; Krogstad *et al.* 1998; LeHew, Guala & McKeon 2010). Concerns about the validity of Taylor's hypothesis

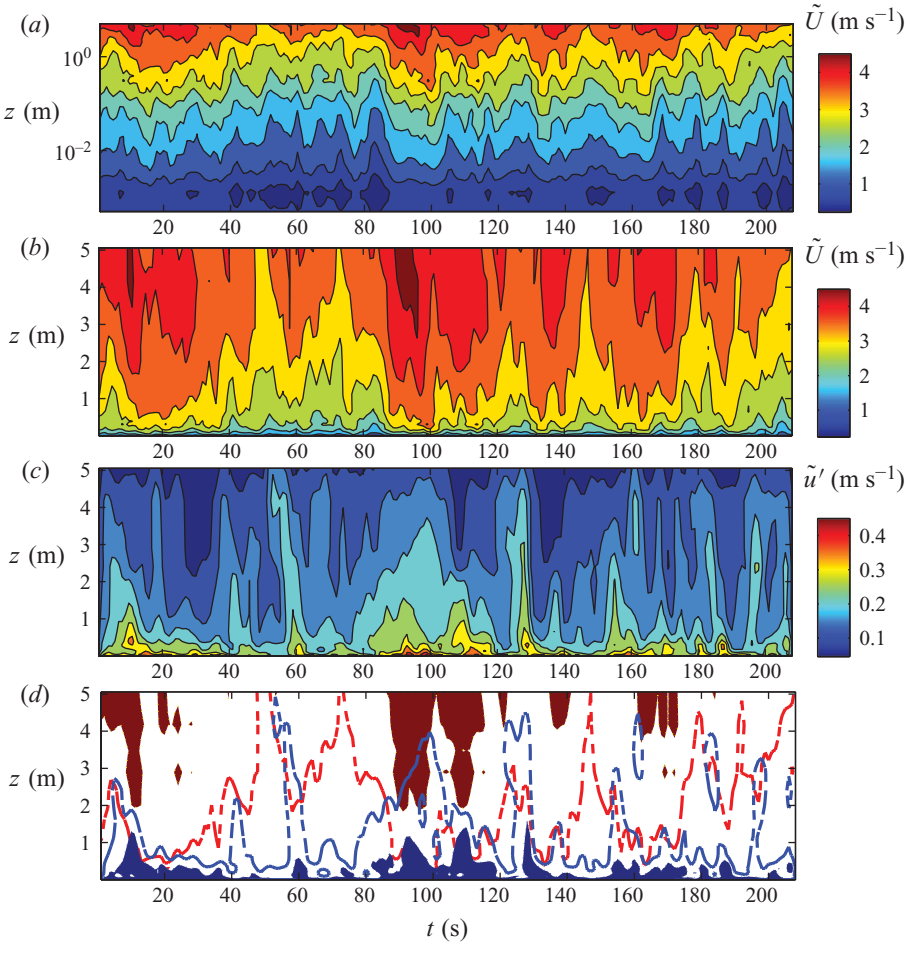

FIGURE 10. (*a, b*) Two-dimensional map of the local mean velocity plotted in logarithmic and linear vertical scale; (*c*) two-dimensional map of the local r.m.s. velocity; in (*d*) a few selected contours of the mean (red) and r.m.s. components (blue) are overlapped. Note that $\tilde{U}$ and $\tilde{u}'$ are obtained from simultaneous measurements at various wall-normal locations z locally averaged according to (4.1).

are amplified at the high Reynolds number in the surface layer: the ratio of mean velocities at the highest and lowest wire locations is approximately 8, suggesting that a conversion between frequency and wavenumber, k, based on a local estimate of the convective velocity at the large scale would lead to a distortion of the effect of a correlated phenomenon in the spatial spectrum that is significantly larger than that observed within and below the overlap layer at lower Reynolds numbers.

According to these arguments, an unambiguous classification of structures and scales based on time history signals should be carried out in the frequency domain in order to prevent contamination by an obvious failure of Taylor's hypothesis. In what follows, we work mostly in the time domain, using frequency filters to provide an objective procedure to analyse the interaction between different scales and distinguish the different populations of turbulent structure. In order to utilize the instantaneous nature of our dataset, we focus on individual runs rather than ensemble averages,

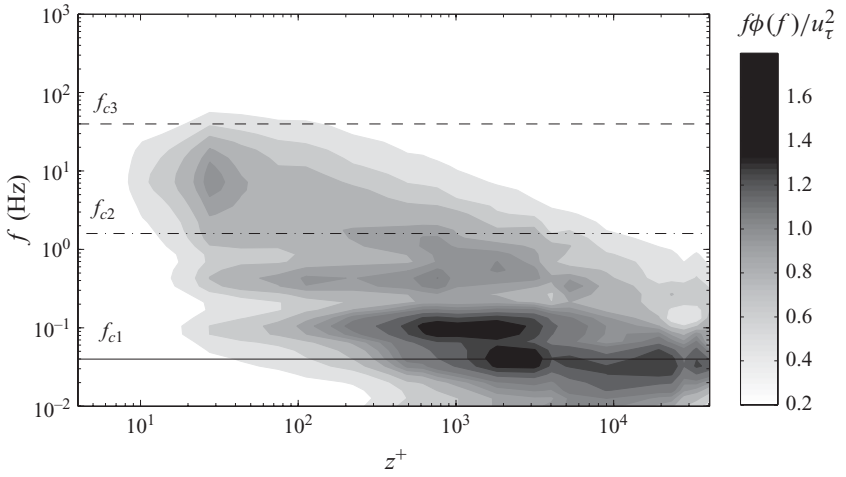

FIGURE 11. Two-dimensional premultiplied spectra, $f\phi(f)/u_\tau^2$ in the $f - z^+$ domain. Horizontal lines indicate cutoff frequencies of $f_c\delta/U(z_{max}) = 0.5$, 20 and 500, respectively.

while ensuring that our results are representative of data acquired under similar conditions during this experimental campaign.

4.2. *Energy distribution across the wall layer*

A quantitative description of turbulent kinetic energy distribution across the wall layer is given by the two-dimensional premultiplied spectrogram shown in figure 11, in which the energy density is plotted as a function of height and frequency for a single data run (the trends are consistent with other runs at similar stability conditions). At this high Reynolds number, two peaks can be detected: one at $z^+ \sim 20$ and high frequency denoting the near-wall turbulent peak, and another located relatively far from the wall, $z^+ = O(10^3\text{–}10^4)$, associated with low frequency and therefore large- and/or very-large-scale motion. The inner and outer peaks reflect the major streamwise energetic activity in a high-Reynolds-number turbulent boundary layer. The inner peak is the signature of the streamwise streaks and longitudinal vortices associated with the near-wall cycle. While its intensity was observed to weakly increase with the Reynolds number, its vertical location is generally accepted to scale in inner units (see Hutchins & Marusic 2007*a* and references therein), implying that the near-wall cycle can be regarded as a universal feature of turbulent boundary layer flows. Since the desert floor has been shown to be a transitionally rough surface, the reduction in the peak energy density associated with the inner peak when compared with smooth wall flows is to be expected (Metzger *et al.* 2007).

The large-scale peak is known to move slowly farther from the wall and broaden with increasing Reynolds number (Hutchins & Marusic 2007*a*), suggesting that the larger the wall region and the inertial sublayer, the more energy can be stored in δ-scale motions and VLSMs. The scaling of the location of the outer peak remains an open question, but is clearly collapsed by neither simple inner nor outer arguments (McKeon 2008; Mathis *et al.* 2009). Unfortunately, this peak is not well resolved in the current set-up (and is also expected to be broad at this Reynolds number). We estimate that the outer peak resides at $z^+ \sim 3 \times 10^3 \pm 2 \times 10^3$, with the caveat that the broad peak observed in figure 11 actually belongs to scales larger than δ but does not allow for a precise distinction between LSM and VLSM.

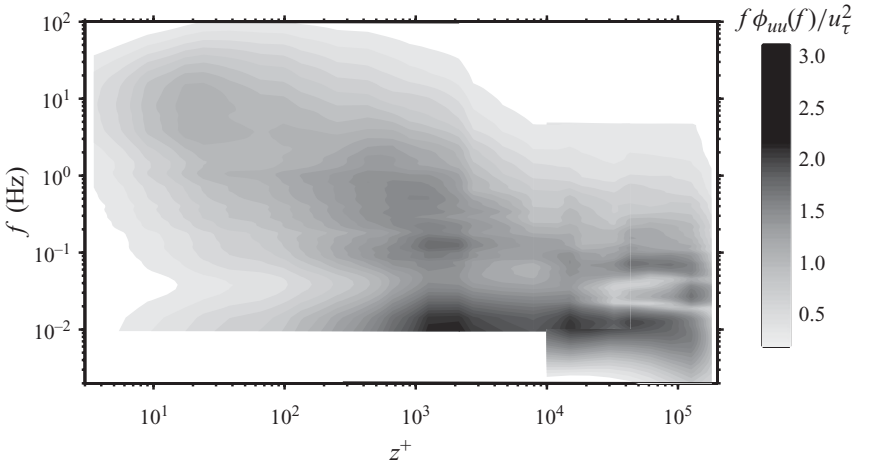

FIGURE 12. Composite premultiplied spectra obtained with measurements by hot wires (four runs) and sonic anemometers (acquisition time between 21:01 and 21:19).

However, by considering a slightly longer sampling period (only slightly relaxing the constraint on stability conditions) and incorporating measurements from the sonic anemometers, a complete spectral description of the flow can be obtained (figure 12). The temporal domain for these measurements covers a near-neutral period of 18 min, with averaging performed over multiple hot-wire runs. Figure 12 illustrates that the results of figure 11 are robust: a large-scale peak is observed at $z^+ \sim 3 \times 10^3 \pm 2 \times 10^3$ for both single and averaged run results. Note, however, that the addition of data obtained further from the wall using sonic anemometers identifies additional large-scale activity in the range of $z^+ \approx 1$–7×10^4, consistent with the observations of Mathis *et al.* (2009) from sonic anemometer measurements alone.

In order to resolve the full spectrum over this range of wall-normal heights, i.e. from the dissipation scales to the VLSM, we would need temporal hot-wire records at least an order of magnitude longer than those available from the present campaign, still within a very near neutral period with limited variation in the wind speed and direction. Even at such a unique site as SLTEST, these requirements are exceptionally strict: thus we cannot fully resolve spectrally the VLSM with a length scale $\gtrsim 6\delta$. Note, however, that the r.m.s. velocity profiles of figure 4(*b*) suggest that there cannot be overly significant energy missing at the largest scales.

On the basis of the spectrogram in figure 11, we can quantify interactions between the different temporal scales by splitting the frequency domain into high- and low-frequency components using simple high-/low-pass filters and providing a comparative analysis of the reconstructed high- or low-pass velocity signal at different heights. The choice of suitable cutoff frequencies is crucial. Note that the hot wire and the sonic anemometer measurements are simultaneous but not located in the same exact spot. Therefore, in order to study scale interactions, we focus hereafter on the hot-wire measurements.

A range of cutoff frequencies to be explored in the subsequent sections are shown by horizontal lines in figure 11 and summarized in table 1. By selecting f_{c1} and f_{c3} as low- and high-pass cutoff frequencies, we focus on the very large scales and the very small scales, respectively. By selecting f_{c2} as a unique low- and high-pass frequency, we split the near-wall energy peak from the large-scale peak, an analysis also performed

Cutoff frequency ID	Frequency (Hz)	$f_cU(z_{max})/\delta$	Filter type	Figures	Section
f_{c1}	0.04	0.5	Low pass	14–16	4.3
f_{c2}	1.4	20	Low pass	17, 18, 19(a)	4.4
$4f_{c1}$	0.16	2	Low pass	19(b)	4.4
$4f_{c1}$–f_{c2}	0.14–1.6	2–20	Band pass	20	4.4
f_{c2}	1.4	20	Low pass	21–23	4.5

TABLE 1. List of the cutoff frequencies used in this paper. The choice of the cutoff is related to the statistical tool employed, it is described in the corresponding section and it contributes to the corresponding figures.

on the spatial spectrum by Metzger & Klewicki (2001) and Hutchins & Marusic (2007*a*). The different statistical methods employed in what follows place different requirements on the filter frequencies: conditional averages (§ 4.3) will be based on a very low cutoff frequency to detect the signature of VLSM; cross-correlations (§ 4.4), focused on the relative phase of the different scales, investigate a range of cutoff frequencies; probabilistic methods (§ 4.5) require a cutoff frequency that preserves the statistical distribution of the quantities investigated.

The wavenumber spectra obtained using Taylor's hypothesis at different heights are shown in figure 13, premultiplied to emphasize inertial scaling regimes and versus kS^*, where the shear scale S^* is approximated by κz in a region of approximate local equilibrium. The figure shows that f_{c3} corresponds to the bottleneck indicative of the end of the inertial subrange/start of the dissipative scales ($k\eta \sim 0.1$, where η is the Kolmogorov length scale) relatively independent of the wall-normal location, a consequence of the wall-normal variations of mean velocity and η. This is further confirmed by the spectra normalized with the Kolmogorov scales (not shown), where the dissipation was obtained by integrating the premultiplied $k^2\Phi(k)$ spectra at each z^+. Similarly, f_{c1} isolates the very low frequencies and is thus related to the VLSM. A cutoff frequency of $f_{c1} = 0.04$ Hz corresponds to $f_{c1}\ \delta/U(z_{max}) = 0.5$ (where $U(z_{max})$ is the velocity at the highest hot-wire measurement location, $z \sim 4.6$ m). In contrast, f_{c2} slides between energetic and inertial scales depending on the wall-normal location, always splitting the VLSMs and the dissipative scales and allowing for a clear distinction between the spectrogram peaks in figure 11. Moreover, as we will see later, f_{c2} can be used within a probabilistic approach that requires comparable probability density functions for the low-pass and high-pass velocities (essentially a filter able to cut the velocity distribution in half). Critically, it does not distinguish between LSM and VLSM structures.

4.3. *A spectral description of the interaction*

In figure 14 we plot the z^+-variation of the low- and high-pass components of the fluctuating streamwise velocity obtained using the f_{c1} and f_{c3} cutoff frequencies, $u_{l1}(t)$ and $u_{h3}(t)$, respectively, offset at each location with the relevant mean velocity. Note the strong temporal coherence of the low-pass signal across the layer. There is clear evidence of the amplitude modulation effect of the large scales on the small-scale activity, as described by Hutchins & Marusic (2007*b*) and Mathis *et al.* (2009), which strengthens closer to the wall. Note that Chung & McKeon (2010) have observed that the magnitude of the apparent modulation is related to the spatial phase relationship of the large and small scales. The large-scale effects on the dissipative scales can also

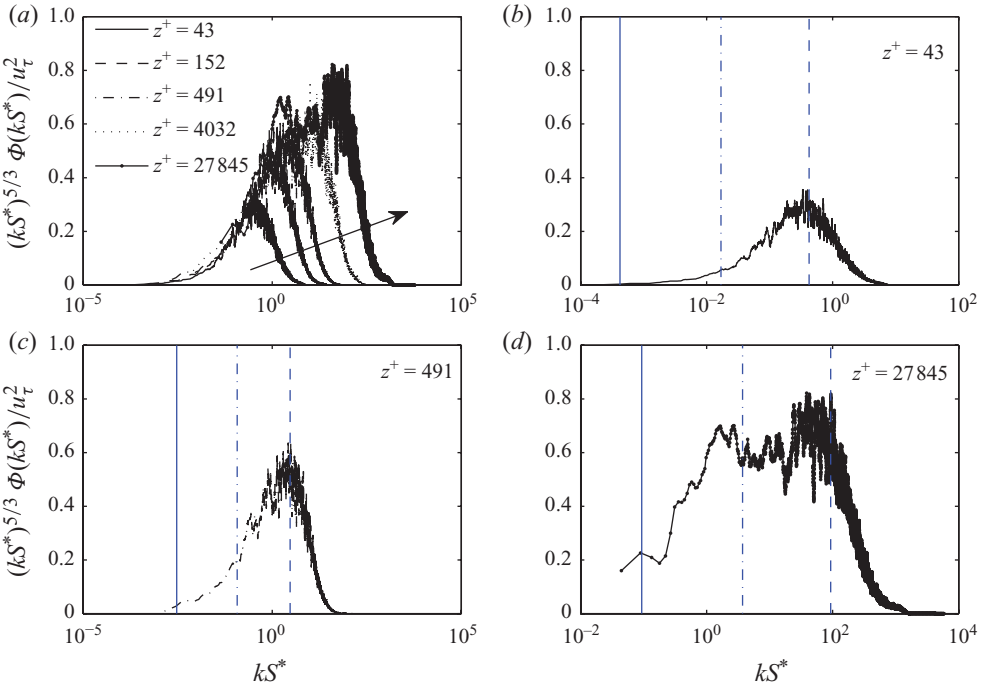

FIGURE 13. (Colour online) Premultiplied spectral density versus wavenumber normalized with the shear scale, S^*. (*a*) Collapse in the inertial subrange at different z^+, increasing in the direction of the arrow. (*b–d*) Single spectra superimposed with the transformed wavenumber filter cutoffs at $z^+ = 43\,490$ and $27\,845$, respectively. The vertical lines correspond to the locations of cutoff frequencies f_{c1-3}, with line styles as given in figure 11.

be observed in figure 15, where the low-pass filtered velocity and dissipation time series are compared (note that dissipation is estimated as $\epsilon(t) = 15\nu(\partial u(t)/\partial t)^2$). In the following, we attempt a quantitative description of this modulation, using spectral and probabilistic analyses.

A possible way to quantify the very-large-scale influence on the smallest scales of motion is to perform a conditional statistical analysis based on the sign of the low-pass velocity signal. In other words, we can identify consistently slow or fast large-scale velocity excursions and make an unambiguous comparison of various statistics computed on those different periods, which should illuminate the strength of the modulation effect.

At each height, the following procedure is implemented.

(*a*) The low-pass velocity signal is divided into continuous subsamples displaying a positive or negative excursion $u_{l3}(z,t)_{+i}$ and $u_{l3}(z,t)_{-i}$, such that each point belongs to the ith positive (negative) subsample $u_{l3}(z,t)_{+i(-i)} > (<)0$.

(*b*) The longest positive and negative subsamples are chosen, denoted by LS^+ and LS^-, respectively, as shown in figure 15(*a*), and then trimmed to equal length.

(*c*) The r.m.s. velocities on LS^+ and LS^-, u'_+ and u'_-, are computed.

(*d*) The power spectra on LS^+ and LS^-, $\Phi(z)_+$ and $\Phi(z)_-$ are computed and normalized to the local turbulent kinetic energy u_+^2 and u_-^2, respectively.

(*e*) The conditioned, premultiplied, two-dimensional power spectral difference $f(\Phi(z)_+ - \Phi(z)_-)/u_\tau^2$ is plotted as a function of height and frequency.

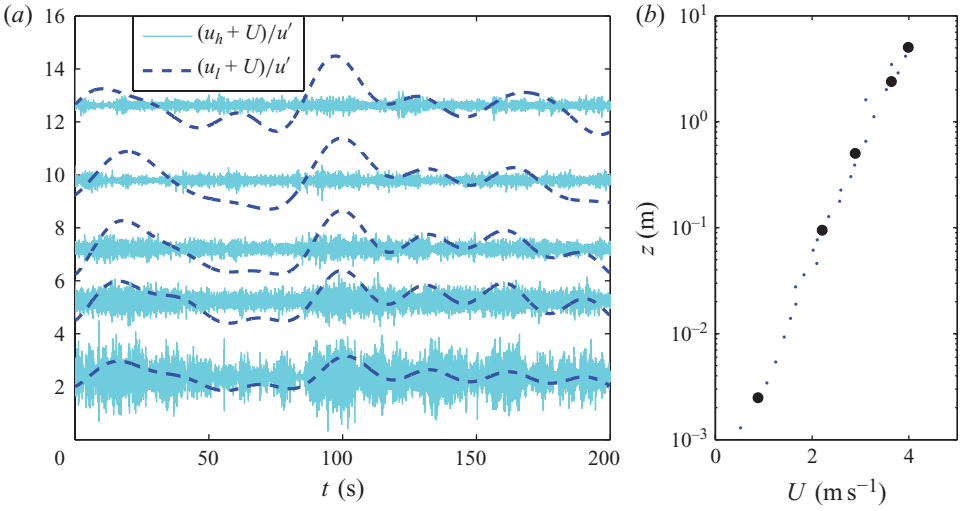

FIGURE 14. (Colour online) (*a*) Wall-normal variation of the low- (f_{c1}) and high- (f_{c3}) pass fluctuating velocities normalized with the r.m.s. velocity, $(u_h+U)/u'$ and $(u_l+U)/u'$ respectively, at $z^+ = 20, 762, 4033, 19\,296$ and $40\,547$. (*b*) Actual wall-normal locations and local mean velocities for the selected wires (•) and other hot-wire probes (·).

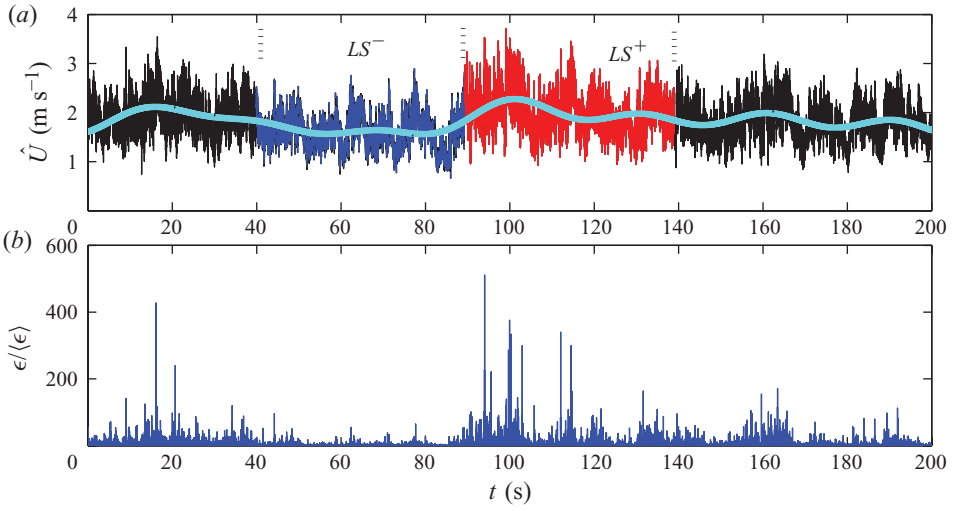

FIGURE 15. (Colour online) Temporal records of the (*a*) streamwise velocity and (*b*) fractional local dissipation at $z^+ = 288$. The low-pass filtered velocity with $f_{c1}\delta/U_\infty < 0.5$ (thick line) leads to the definition of two periods LS^+ and LS^-, representing the largest continuous positive and negative excursions with respect to the mean velocity value, respectively.

The spectral difference, or the difference in energy distribution across frequencies between the LS^+ and LS^- samples, is presented in figure 16. Most of the difference between LS^+ and LS^- periods is found close to the wall, in the region $z^+ < 10^3$, in particular at the high frequencies/small scales at $z^+ = O(10^2)$, with a secondary peak at around $z^+ = 400$. The near-wall turbulent intensity peak identified in figure 11 is most strongly affected by the large-scale features of the flow identified here. In

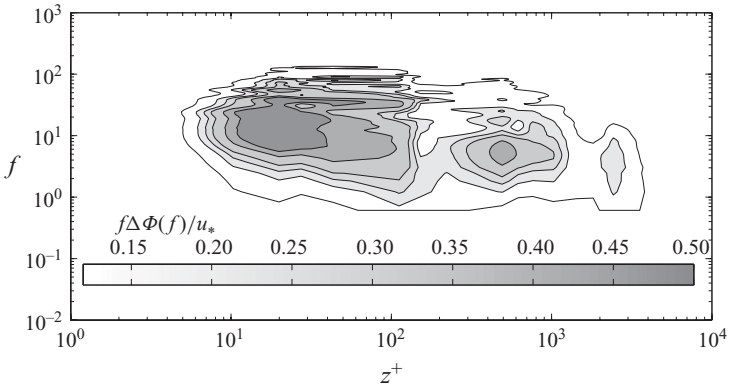

FIGURE 16. Conditioned two-dimensional, premultiplied power-spectral difference between time periods LS^+ and LS^-, i.e. $f(\Phi(z)_+ - \Phi(z)_-)/u_\tau^2$ in the $f - z^+$ domain.

broad terms, the large-scale amplitude modulation trends indicated in figure 16 are dominated by the combination of long coherent LS^+ periods (where the low-pass filtered velocity is larger than the mean velocity) associated with higher small-scale turbulent intensity, and vice versa for the LS^- period. Note however that the results of Mathis *et al.* (2009) suggest that this trend should reverse further from the wall.

These results support the now broadly accepted idea that a scale other than the one representative of near-wall structure must contribute to the turbulence intensity at the wall. The fact that similar trends in the Reynolds number dependence of the near-wall fluctuating velocity, $u'^+(z^+ \sim 20)$, are observed in both smooth and rough wall flows (see Metzger & Klewicki 2001) suggests that the modulation effects are relatively independent of the condition of the near-wall turbulence (which is affected by the surface characteristics) and must therefore be related to an 'outer-like' scale, perhaps through a 'top-down' type of interaction (Hunt & Morrison 2000).

4.4. *Relative phase of the filtered signals*

The spectral analysis described above does not emphasize whether there is a relative spatial/temporal phase shift between the footprint of the large-scale structure and the response of the high-pass velocity or dissipation fields. A statistical answer to this question can be provided by developing the analysis proposed by Bandyopadhyay & Hussain (1984). The procedure can be summarized into the following steps.

(*a*) The velocity signal at each height is low-pass filtered with a cutoff frequency f_c.

(*b*) The absolute value of the high-pass filtered signal u_l is low-pass filtered back with the same cutoff frequency f_c and the mean value subtracted. The two signals represent a large-scale (low frequency) velocity signal u_l and a large-scale envelope (or modulation) of the high-frequency signal $u_{l,e}$, respectively (note that the latter is denoted by u_h in Bandyopadhyay & Hussain 1984);

(*c*) The signals u_l and $u_{l,e}$ can be then cross-correlated and normalized with the product of the respective standard deviations, here denoted by u'_l and $u'_{l,e}$.

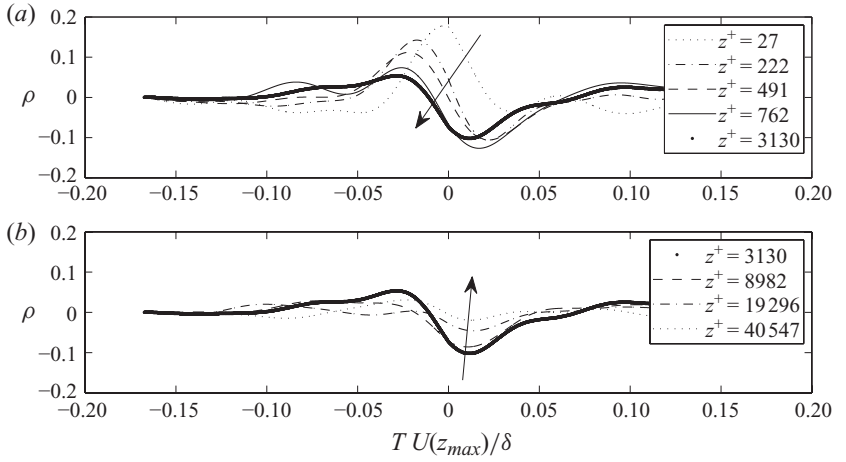

FIGURE 17. (*a*, *b*) Cross-correlation, ρ, between the low-frequency signal and the envelope of the high-frequency velocity, u_l and $u_{l,e}$ respectively, at different z^+ locations (cutoff frequency set as f_{c2}).

(*d*) The time lag at which the cross-correlation, ρ, peaks provides a statistical measure of the lead (or lag), T, of one signal with respect to the other. Here

$$\rho(z^+, T, f_c) = \sum_t \frac{u_l(t, z^+)u_{l,e}(t + T, z^+)}{u'_l(z^+)u'_{l,e}(z^+)} \tag{4.2}$$

and a positive value of T indicates that u_l leads $u_{l,e}$, denoted as a positive phase difference.

The only user-imposed parameter is f_c, implying that the large and small scales are only defined by means of one cutoff frequency. On the basis of the spectrogram in figure 11, we first choose $f_c = f_{c2}$ to unambiguously separate the two spectral peaks. Given the limited vertical extent of our measurements and the uncertainty in δ, normalization of the frequency is performed using the maximum height $z_{max} = 4.6$ m and the associated mean velocity $U(z_{max}) = 3.98\ \mathrm{m\,s^{-1}}$. Note that this analysis identifies only the phase relationship between scales either side of the cutoff frequency at each wall-normal location and not the relative phase of the large scales as z^+ varies. However, the latter is expected to be small (in the layer investigated here), as observed from the small variation with z^+ of the very-large-scale velocity signals shown in figure 14(*a*).

Examples of the variation of ρ with wall-normal distance are given in figure 17. As discussed by Bandyopadhyay & Hussain (1984), a single positive (negative) peak in ρ at $T = 0$ corresponds to signals that are locally fully in (out of) phase, while the existence of both positive and negative peaks that are antisymmetric about $T = 0$ implies that the signals are about 90° out of phase. Figure 17 suggests that very near the wall ($z^+ = 27$), the envelope of the small scales is substantially in phase with the larger scales, while at almost all points further from the wall, $u_{l,e}$ leads u_l by a phase angle that reaches about 90° at a wall-normal location $z^+ \sim 10^2$–10^3. Note that the absolute magnitude of the correlation peak reflects interactions across a range of scales dictated by the filter.

The contour plot of figure 18 confirms the picture of the variation in the phase shift across the wall layer. The time shifts corresponding to clear maxima and minima of

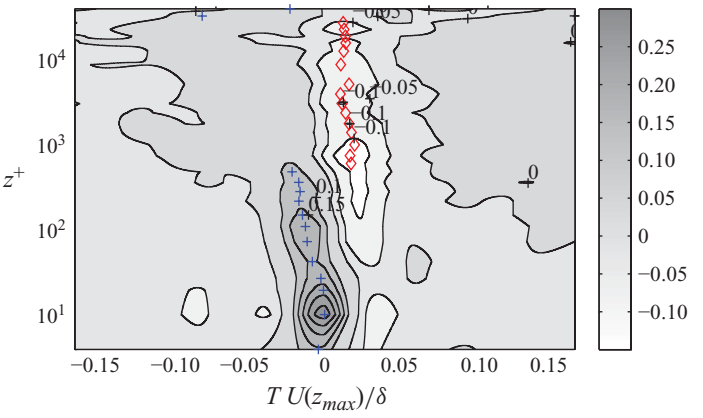

FIGURE 18. (Colour online) Contour plot of the wall-normal variation of ρ, the cross-correlation between the low-frequency signal and the envelope of the high-frequency velocity, u_l and $u_{l,e}$, respectively (cutoff frequency set as f_{c2}), at different z^+ locations. Symbols: + and $\diamond$ denote the location of the (dominant) maximum and minimum values of ρ, respectively.

the cross-correlations at each wall-normal location are shown by cross and diamond symbols, respectively. Qualitatively, we confirm the observations of Bandyopadhyay & Hussain (1984) at a Reynolds number of $Re_\tau \sim 2 \times 10^3$ that the small scales very slightly anticipate the larger scales in the wall and buffer regions, while the signals move out of phase in the overlap layer. Since the present dataset does not extend beyond the overlap region, we cannot investigate the behaviour in the outer region, but we note that Bandyopadhyay & Hussain (1984) observed that the large scales tend to lead small scales in the outer region. Note that our normalizations of f_c and T differ from those used in Bandyopadhyay & Hussain (1984), who selected the cutoff frequency based on the expected burst frequency in a laboratory boundary layer. However, the overall results are remarkably similar despite a Reynolds number disparity of close to two orders of magnitude.

Bandyopadhyay & Hussain (1984) related this scale interaction to δ scale, ramp-like structures. We note that our f_{c2} is unlikely to divide cleanly the effects of the hairpin and VLSM paradigms and as such our results must be interpreted with both structures in mind. The close agreement between the laboratory and ASL results near the wall suggests that the interaction in this region is governed by inner scaling.

The region in which the small-scale envelope leads the large scales with a $\sim 90^\circ$ angle has particular significance to recent studies on the location of the reversal in the sign of the amplitude modulation, determined by use of the Hilbert transform by Mathis *et al.* (2009) and filtering of large-eddy simulation data at a high Reynolds number by Chung & McKeon (2010). Both the above techniques will indicate zero amplitude modulation when the phase difference is $\sim 90^\circ$. Mathis *et al.* (2010) have hypothesized that this point, z_0^+, corresponds to the wall-normal location at which the energy associated with the VLSMs peaks and the reversal in the sign of the skewness of u. Our estimate of $z_0^+ \sim 10^3$–10^4 is in good agreement with the estimate of the location of the spectral peak in figure 11. Similarly, $z_0^+ \sim 10^2$ from the Bandyopadhyay & Hussain (1984) results at $Re_\tau \sim 2 \times 10^3$ corresponds well with the location of the outer energy peak ($z^+ \sim 60$) in the $Re_\tau \sim 10^3$ boundary layer of Hutchins & Marusic (2007*b*).

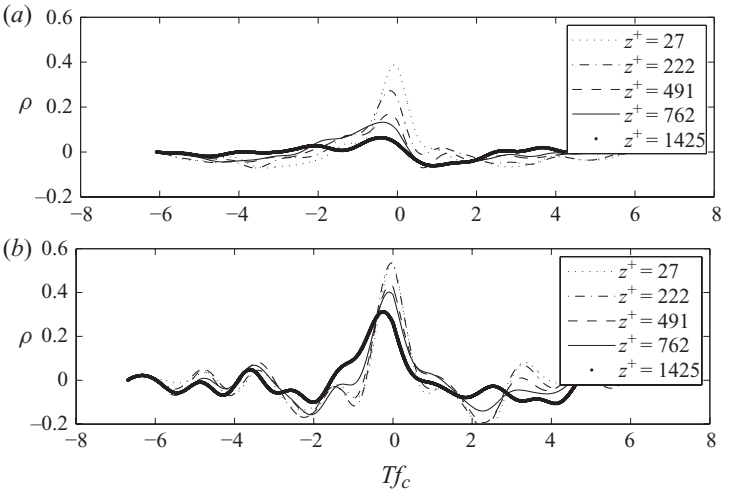

FIGURE 19. Cross-correlation, ρ, between the low-frequency signal and the envelope of the instantaneous dissipation, u_l and $\epsilon_{l,e}$ respectively, at different z^+ locations and cutoff frequencies (a) f_{c2} and (b) $4f_{c1}$. Note that the normalizing frequency f_c for the time axis is always chosen as the low-pass (and envelope) frequency.

Another interesting question is the phase difference between the large scales and the dissipative scales, which must respond to the local changes in spectral density on some time scale. We repeat the procedure above using the instantaneous dissipation time series (instead of the high-pass filtered velocity), consistently obtaining the large-scale envelope with a low-pass filter with cutoff frequency f_{c2}. The correlation curves are shown in figure 19(a). The peak is more pronounced but less broad compared with figure 17(a), with no strong evidence of a phase shift. Essentially, the peak vanishes with increasing z^+, confirming that dissipation is locally affected by the large scales especially close to the wall. In figure 19(b), we move the low cutoff frequency filter from f_{c2} towards f_{c1}, specifically down to $4f_{c1}$. The choice of $4f_{c1}$ was dictated by the convergence of the cross-correlation curves; with a longer sample, f_{c1} would have been the ideal choice. The comparison between the two panels suggests that dissipation is strongly influenced by the VLSM over a larger range of z^+ than by the LSM. This is consistent with the results of the conditioned spectra, with the comparison between the dissipation and the f_{c1} low-pass filtered velocity time series shown in figure 15, and with the results of Guala *et al.* (2010) concerning structure functions.

Lastly, we investigate the VLSM–LSM phase relationship by retaining the low-pass cutoff frequency used for the VLSM ($4f_{c1}$) and a band-pass filter for the LSM, specifically using the frequency range delimited by $4f_{c1}$ and f_{c2}. The results are presented in figure 20. The interaction is essentially non-local and persistent up to $z^+ \sim 10^4$, with no appreciable phase reversal. Indeed, the envelope of the LSM appears to lead the VLSM signature across the whole layer. We summarize the phase relationship between the scales investigated as follows. The dissipative scales are locally governed by both LSM and (mostly) VLSM, especially close to the wall. On the contrary, VLSM and LSM seem to be out of phase with no significant variation in z^+.

The phase shift observed in figure 17 with a simple f_{c2} cutoff frequency can thus be reinterpreted in view of the trends outlined in figures 19 and 20. As a

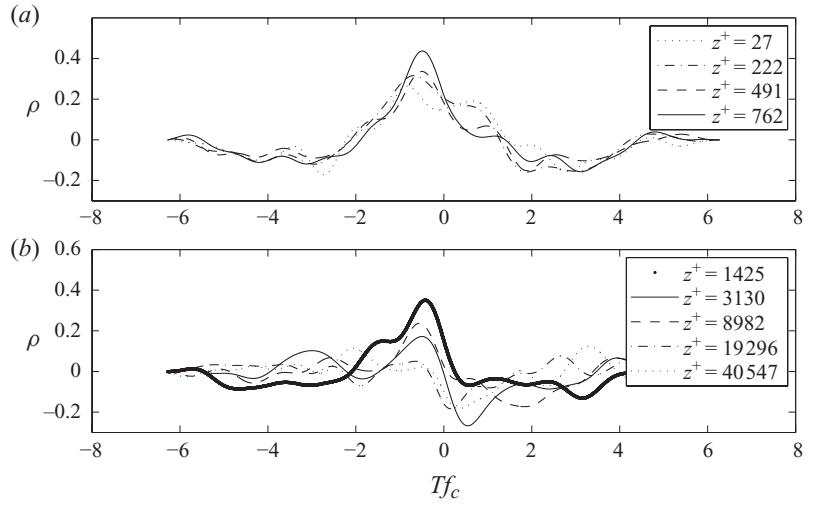

FIGURE 20. (a, b) Cross-correlation, ρ, between the low-frequency signal and the envelope of the band-pass filtered velocity, u_l and $u_{l,e}$ respectively, at different z^+ locations. The band-pass filter is set between $4f_{c1}$ and f_{c2}, such that the signal represents the LSM with limited contamination by the VLSM. The normalization is consistent with figure 19.

working hypothesis, we have divided the frequency domain into three sets, each set related to a possible structural type, namely the VLSM in the low frequencies, the dissipative scales in the high frequencies and the LSM in the intermediate frequencies. It is noteworthy that while the frequency f_{c2} marks a clear cut between VLSM and the small scales, the LSM contribution is likely to remain somewhat split. In the spectrogram in figure 11, as we move along the f_{c2} cutoff with increasing z^+, the contribution to the streamwise kinetic energy of the low frequencies, relative to the high frequencies, progressively increases. Therefore, we can argue that in the $f > f_{c2}$ domain the dominant contribution to $u_{l,e}$ is given by the small scales close to the wall, and by the LSM far from the wall. If we assume that the VLSM governs the $f < f_{c2}$ domain, predominantly contributing to the behaviour of u_l, then we can interpret the phase shift of figure 17 as a structural change across the vertical direction. Indeed, close to the wall, both VLSM and LSM are in phase with the high-frequency components (figure 19). Farther from the wall, as the VLSM starts to interact with the larger scales that start contributing to $u_{l,e}$, a progressively out of phase relationship is observed (figure 20). The variation of the phase shift with z^+ can be accordingly discussed in a general picture where (i) the small scales in the near-wall layer are strongly affected by VLSM, locally in time and space; (ii) a region centred on $z^+ = 10^3$, not exceeding $z^+ = 10^4$, is characterized by the out of phase, possibly cyclic, interaction between VLSM and LSM; (iii) the layer above $z^+ = 10^4$, where the interaction is weak, suggests that the VLSMs are the statistically dominant population (in agreement with Chung & McKeon 2010).

4.5. *A probabilistic description of the interactions*

Additional information can be obtained from a probabilistic description of the large-scale/small-scale interactions. In this analysis, the low-pass and the high-pass reconstructed velocity signals are interpreted as two distinct variables in order to investigate statistics conditioned on the large-scale (low pass) velocity magnitude. The chosen cutoff frequency, f_{c2}, includes the energetic contribution from the VLSM

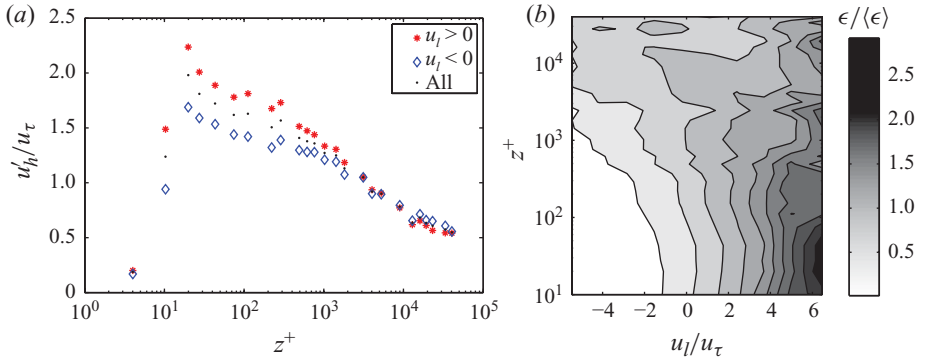

FIGURE 21. (Colour online) (*a*) Comparison between the normalized high-frequency turbulent intensity profiles u'_h/u_τ obtained in regions of positive and negative excursions of the low-pass filtered velocity $u_l > 0$, $u_l < 0$, respectively, and (*b*) conditional averages of $\epsilon/\langle\epsilon\rangle$ in the z^+, u_l/U plane. Note that the cutoff frequency is set as f_{c2}.

in u_l, while also preserving a genuine $PDF(u_l)$ that is required for the probabilistic analysis.

The energy associated with high-frequency velocity fluctuations, u_h^2, is significantly affected by the sign of u_l, as shown in figure 21(*a*). This is in agreement with the lower-Reynolds-number results of Hutchins & Marusic (2007*b*), although at this high Reynolds number we observe both that $u_{h+}^2 > u_{h-}^2$ for $z^+ \lessapprox 6 \times 10^3$ and a slight reversal of the magnitudes for larger z^+, consistent with the phase observations of the previous section, although this observation may not be significant relative to the experimental accuracy.

The time resolution of our measurements also allows us to interrogate the temporal variation of the dissipation. Figure 15 gives a visual comparison between the large-scale velocity signal and the local dissipation, ϵ as a fraction of the mean dissipation, $\epsilon/\langle\epsilon\rangle$. Here ϵ is determined using the one-dimensional approximation and the local streamwise acceleration. The conditional average shown in figure 21(*b*) underscores that ϵ increases with increasing magnitude of u_l (at each z^+) and vice versa, such that it can be inferred that the influence of the very large scales extends down to the smallest, dissipative scales, in particular in the region close to the wall. Since the majority of the dissipation is concentrated in the near-wall region, it can be concluded that a high level of dissipation across the wall layer is more likely to occur when the large-scale velocity close to the wall is in its positive excursion with respect to the mean value.

We further investigate the mutual occurrence of the fractional local dissipation $\epsilon/\langle\epsilon\rangle$ and large-scale velocity magnitude u_l using joint probability density functions (JPDFs). It is worth noting that JPDFs are the backbone of mutual information content analysis, thus particularly suited for studying interactions (see e.g. Poggi *et al.* 2004).

The $JPDF(u_l/U, \epsilon/\langle\epsilon\rangle)$ at a fixed $z^+ = 46$ is shown in figure 22. A comparison with the symmetric distribution given by the product of the PDFs, $PDF(u_l)/U)\,PDF(\epsilon/\langle\epsilon\rangle$, shows that the JPDF is significantly tilted relative to a representation of independent distributions. The JPDF shows the mutual distribution and hence the interactions between the two variables.

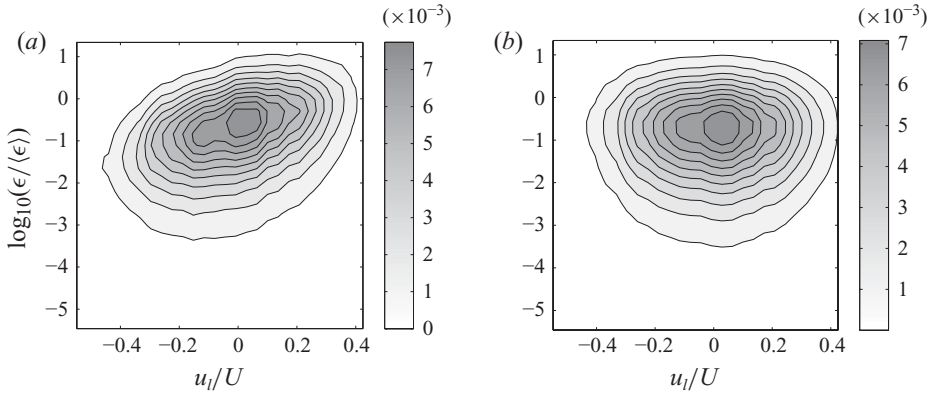

FIGURE 22. Distributions of the dissipation and the large-scale velocity (cutoff frequency set as f_{c2}) at $z^+ = 43$: (*a*) $JPDF(u_l/U, \epsilon/\langle\epsilon\rangle)$ and (*b*) $PDF(u_l/U)\,PDF(\epsilon/\langle\epsilon\rangle)$.

The normalized JPDF/PDF ratio, ξ, where

$$\xi = \frac{JPDF(u_l/U, \epsilon/\langle\epsilon\rangle)}{(PDF(u_l)/U)\,PDF(\epsilon/\langle\epsilon\rangle)} \tag{4.3}$$

is a probabilistic measure of the interaction between the two variables, independent of their respective distribution. We show the normalized JPDFs, ξ, at different heights in figure 23. Consistent with the signature of the positive large-scale velocity excursions on the conditioned spectra, we note that the distribution of (rare) high and low dissipation events at the small scales appears strongly modulated by the large-scale fluctuations of u_l, with the magnitude of this modulation decreasing as the distance from the wall is increased. At $z^+ = 4 \times 10^4$, the distribution of high dissipation events no longer depends on u_l, while low dissipation events still show a weak preferential distribution.

5. Discussion

Several aspects of the high-Reynolds-number results described require a revisiting of the prevailing structural framework of boundary layer turbulence developed in the last few decades and based on experimental results at the laboratory-scale Reynolds number.

(*a*) While the isocontours of the two-point correlations with a reference probe location close to the wall reflect the typical signature of ramp-like structures observed across a range of Reynolds numbers, a significant difference was observed when the reference probe was far from the wall, but still within the overlap layer, $z/\delta \ll 0.1$ (figures 7 and 8). There appears to be evidence of coherence with limited phase variation in the wall-normal direction further from the wall, $z^+ \gtrapprox O(10^3$–$10^4)$, in agreement with suggestions from the higher laboratory Reynolds number results of other authors in turbulent boundary layers and channels (Tutkun *et al.* 2009).

(*b*) The apparent amplitude modulation of the smaller scales by the larger scales is observed to vary with wall-normal distance, reducing significantly for $z^+ \gtrapprox 10^3$ (figures 16 and 21). Further effects of scale interactions, such as phase-shift variation in the cross-correlation functions (figures 19 and 20) and the preferential distribution of strong dissipative events (figure 23) seem to characterize a well-confined layer of $z^+ \lessapprox 10^4$, suggesting that above it some structural changes are expected. Such a trend

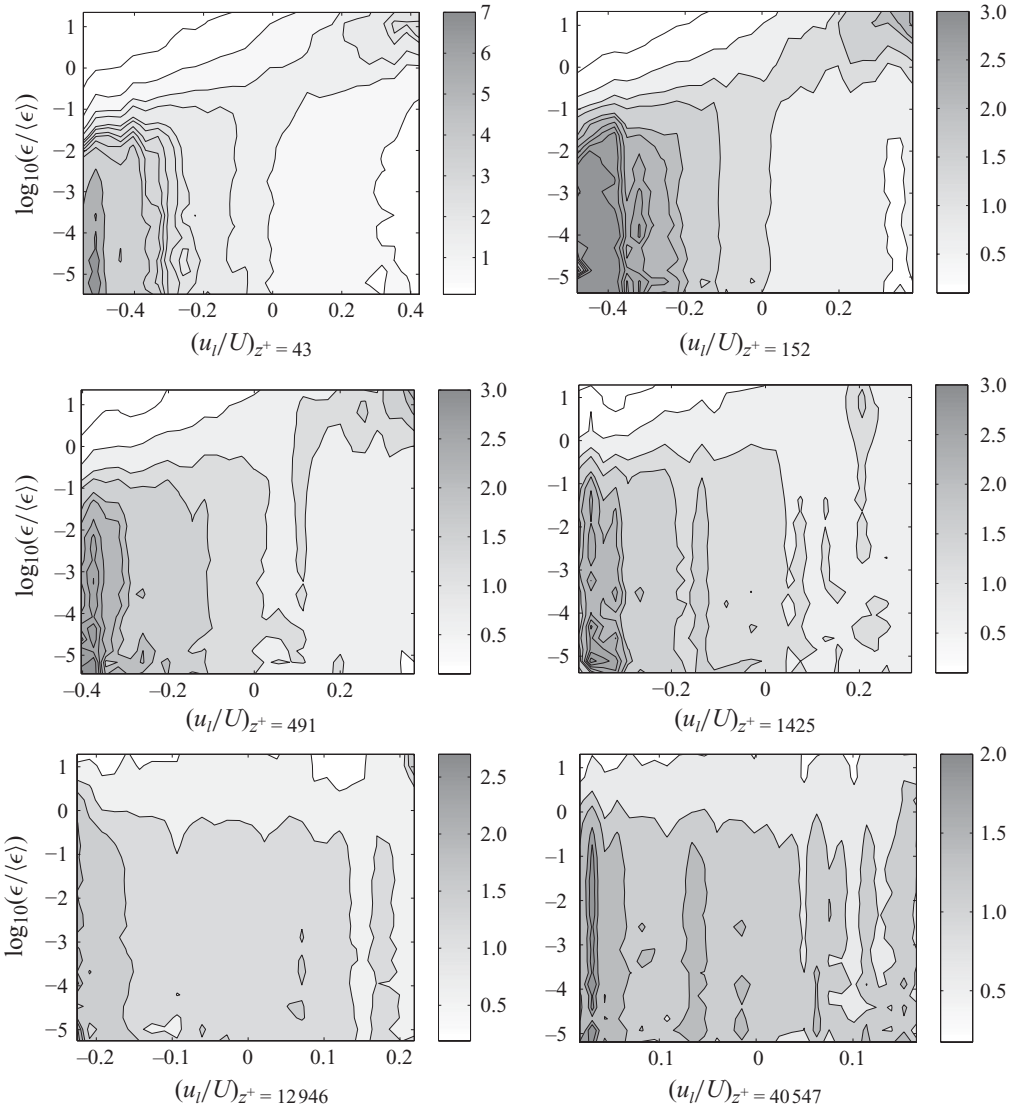

FIGURE 23. Normalized JPDFs of the large-scale velocity (cutoff frequency set as f_{c2}) and local dissipation, $\xi = JPDF((u_l)/U, \epsilon/\langle\epsilon\rangle)/((PDF(u_l)/U)\,PDF(\epsilon/\langle\epsilon\rangle)$ at different heights from the wall. Note that the contour levels change from panel to panel, as the maximum values decrease with z^+.

is consistent with the results of Guala *et al.* (2010), who outlined a very-large-scale modulation of the multiscaling behaviour of the velocity structure functions (and thus of the intermittency of the velocity signal), again mostly confined to the region $z^+ < 10^3$.

(*c*) The localization of the temporal phase-shift reversal (figure 18) seems to be invariant with the Reynolds number (see the comparison with Bandyopadhyay & Hussain 1984), suggesting that the type of structures responsible for such a trend may occupy similar regions of the boundary layer when described in inner units. However, when the focus is shifted solely to the effect of the VLSMs, the cross-correlation plots

reveal that the modulation can be in phase (on the dissipative scale) or out of phase (on the large scales), but mostly confined to a layer of the order of thousands of viscous wall units.

In what follows we develop a possible interpretation of these results, based on the working hypothesis that a class of very-large-scale 'structures' with statistical signatures consistent with VLSMs exists at a high Reynolds number and can be observed in the streamwise velocity field of the turbulent boundary layer, in addition to the dominant ramp-like structures of wall turbulence usually described in terms of the hairpin-packet paradigm.

5.1. *On hairpin packets and ramp-like structures*

We begin by detailing the limits and relevance of the hairpin conceptual model in high-Reynolds-number turbulent boundary layers. While the model was developed from low-Reynolds-number observations of hairpin vortices, packets and bulges, the surface layer offers unique scale separation, which amplifies differences between inner and outer scalings (but also requires *a priori* knowledge of the form of the scalings in order to observe them).

Hairpins are typically described as three-dimensional vortical structures consisting of a semiarch (the head) attached to two streamwise vortices (the legs) that reside below and downstream of the head (see e.g. Theodorsen 1952; Acarlar & Smith 1987; Adrian *et al.* 2000; Ganapathisubramani, Longmire & Marusic 2003; Ganapathisubramani, Longmire & Marusic 2006). They are perhaps the prototypical example of eddies that are attached to the wall. A signature of the hairpin head commonly captured by PIV measurements consists of a spanwise vortex of diameter less than $100\nu/u_\tau$. Hairpins have been observed to be organized in larger, ramp-like structures with an inclination angle of about 10°–13° to the wall (e.g. Christensen & Adrian 2001), extending up to the top of the boundary layer. It has been proposed that the hairpin aggregation mechanism is based on their mutual induction and spanwise alignment (Adrian *et al.* 2000).

Despite the apparent ubiquity of hairpins in the experiments described above and, more recently, in the direct numerical simulation of Wu & Moin (2009), conclusive evidence of their existence has not been detected in the ASL, for example in the studies of Hommema & Adrian (2003) and Morris *et al.* (2007). Ramp-like shear layers, however, were observed in both these ASL studies in the region of $z^+ < 10^3$. While insufficient spatial measurement resolution may have contributed to the apparent lack of hairpins, it is a valid question whether there is a limit to the coherence of these structures with the Reynolds number, such that they would not be expected to exist in the ASL to the same extent as in the wind-tunnel studies. In other words, do we expect the signatures of ramp-like structures and aligned hairpin vortices to extend up to the full surface layer height, $\delta \approx 50$–100 m? Similarly, do we expect the laboratory-observed, self-sustaining, mutual induction mechanism, which was hypothesized to generate hairpin structures in the region $z/\delta \lesssim 0.1$, to scale on outer units in the ASL, where the vertical extent would correspond to about 5–10 m? The suspicion that some structural differences between wind-tunnel studies and ASL field measurements should be expected based on the difference in Reynolds number was also pointed out by Adrian (2007). He noted that the existence of hairpin packets requires vortices so 'organized and undisturbed' that the self-sustaining mechanisms could be efficient much further from the wall than the $400\nu/u_\tau$ investigated numerically by Zhou, Adrian & Balachandar (1996) and Zhou *et al.* (1999).

The present results offer some statistical evidence for features associated with the hairpin paradigm. Figures 7 and 9 support the Reynolds number invariance of the structural angle observed by Marusic & Heuer (2007) and identify coherence with a signature reminiscent of the ramp-like structures associated with hairpin packets at a lower Reynolds number. In addition, in the same region of the order of thousands of viscous wall units, similar results in terms of the temporal phase relationship between the small and large scales are observed here and in the lower-Reynolds-number studies of Bandyopadhyay & Hussain (1984) (figure 17). Thus, the robustness of inner scaling features appears to be Reynolds-number-independent, with the accompanying conclusion that the structure associated with this region and the auto-generation arguments of Zhou *et al.* (1996, 1999) should also be essentially independent of the Reynolds number. Thus, there appears to be statistical evidence that hairpin vortices and hairpin packets should exist in high-Reynolds-number wall turbulence, a claim that requires further investigation and is a topic of ongoing research.

5.2. *On the very large scales of motions*

While the above results suggest that the organization of some turbulent structures seems to be invariant with the Reynolds number in a layer close to the wall, say $z^+ \lesssim 10^4$, the same layer also appears to be populated by the VLSMs. These are clearly observed in the spectrogram in figures 11 and 12 without an upper bound in our vertically limited dataset, and in the visualization in figures 10 and 14. In the proposed picture of the high-Reynolds-number turbulent boundary layer, the VLSMs are regarded as one of the statistically dominant and active structural populations across the whole wall layer (at least up to $z^+ = 4 \times 10^4$ so far investigated). Their footprint penetrates down to the wall, in agreement with lower-Reynolds-number results, with a strong modulating effect across a range of scales, from the dissipative ones (see figures 15, 21 and 23), up to the scale of the energy-containing eddies (see figure 16). Along with amplitude modulation effects, the phase relationships between the very large scales (obtained by low-pass filtering the velocity signal) and the envelopes of the high-pass filtered velocity suggest a complex signature: a local (in time and space) interaction between VLSMs and the dissipative scales close to the wall, and an out-of-phase interaction between VLSMs and some other large-scale features addressed as LSM, extending farther from the wall. Major changes in the vertical distribution of dominant structural populations are indeed reflected in a different interaction with the VLSMs. In particular, we discuss here the relationship between the ramp-like attached structures and the VLSMs. The vertical extent of the layer where scale interaction is mostly observed, up to $z^+ = O(10^3)$, appears consistent with the location at which the two-point correlations of figures 7 and 8 highlight a change of signature in the statistically dominant structure. This leads to the major hypothesis, formulated here, in the phenomenological interpretation of scale interactions: hairpins and hairpin packets are consistent with the attached eddy model in the near-wall layer, up to $z^+ = O(10^3)$; in the very same layer, these attached structures coexist and strongly interact with a population of VLSMs permeating the whole wall region.

It is noteworthy that the typical phenomenological picture of spanwise meandering VLSMs coexisting with structures from the hairpin paradigm in the wall region, arising from lower-Reynolds-number experiments, is not in contradiction with the conceptual model provided above. A close examination of the implications of the scale separation achievable in the ASL reveals that there must be differences from the low-Reynolds-number picture associated with the vertical extent of both structure

types, likely concerning the relative importance of the constraining effect of the outer edge of the boundary layer. Essentially, the VLSMs at a high Reynolds number are free to extend further in the wall-normal direction than hairpin packets, while at a lower Reynolds number both structures can occupy the whole boundary layer height. Therefore, while the VLSMs at low–moderate Reynolds number are associated with bulges of ramp-like structures (Kim & Adrian 1999; Guala *et al.* 2006; Balakumar & Adrian 2007), the VLSMs at a high Reynolds number appear, so far, to be a distinct population from the ramp-like structures (though interactions obviously occur and cause–consequence relationships must still be addressed). A deeper understanding of the formation of large- and very-large-scale structures in general will almost certainly further illuminate the relationship between hairpin packets and the VLSMs and will shed some light on the definition of LSM at high Reynolds numbers.

6. Conclusions

This paper addresses some structural aspects of high-Reynolds-number turbulent boundary layers, based on experimental data obtained in the very nearly neutral atmospheric surface layer. While the limitations of this type of dataset have been acknowledged, the flow has been widely accepted as representing the sole model of a truly high-Reynolds-number canonical zero-pressure-gradient turbulent boundary layer, and an exhaustive statistical and spectral description of the present data validates this assumption. The synchronous nature of the measurements permits analysis of the streamwise velocity in the temporal/wall-normal domain and characterization and quantification of the interactions between scales in the wall region. As a direct consequence of the large Reynolds number, $Re_\tau \simeq 5 \times 10^5$, such interactions are addressed in a flow where the inner and outer scales are clearly separated.

Different statistical and observational tools have been used to infer the characteristics of different structural groups, and their interactions both with each other and with small-scale activity across the whole wall-normal measurement domain. A spectral analysis focusing on the comparative activity between regions characterized by the positive (LS^+) and negative (LS^-) excursions of the low-pass velocity (faster and slower than the mean, respectively) revealed a significant variation in the near-wall turbulent intensity peak of the spectrogram ($z^+ \simeq 20$), confirming the strong amplitude modulation effect of the very large scales on the wall region proposed by Hutchins & Marusic (2007*b*) and Marusic *et al.* (2010). At this Reynolds number, the strongest modulation is confined to a near-wall layer, $z^+ < 10^3$, although a non-negligible effect was observed up to $z^+ \sim 10^4$. The modulation is concentrated in the high frequencies/small scales.

The excellent temporal resolution of the hot-wire data permitted investigation of the modulation effect down to the smallest scales, finding a strong signature in the energy dissipation. A probabilistic analysis shows that both the conditional average of dissipation and the distribution of rare strong dissipative events show a clear preferential pattern during positive large-scale velocity excursions (high dissipative events are three times more probable as compared to negative events). It is noteworthy that the vertical distribution of scale interaction effects, which can also be interpreted in terms of the spatial phase relationship, is confined in a wall layer of the order of thousands of viscous wall units, seemingly not exceeding $z^+ = 10^4$, consistent with similar observations of the multiscaling behaviour of the velocity differences (Guala *et al.* 2010).

A phenomenological interpretation of our results assumes the existence of both hairpin-like structures near the wall and a population of very-large-scale turbulent structures, the VLSMs, throughout the whole layer. Indeed, distinct signatures of hairpin (and hairpin packet) type structures and VLSMs were inferred in the two-point correlations of the streamwise velocity, in the structural inclination angle, in the spectral domain and in the phase relationship between the small and large scales, all in agreement with several contributions in the literature. The scale separation achieved in the ASL allows unfolding of structural similarities and differences with wind-tunnel studies, and thus reinterpretation of previous observations in the unambiguous context of the high-Reynolds-number turbulent boundary layer. Both VLSMs and hairpins have previously been shown to be 'active' in the sense of contributing significant shear stress and both result in a signature of coherent regions of a uniform streamwise momentum. While the scaling of the VLSMs remains an open question (beyond resisting either simple outer or inner arguments), the hairpin-packet model appears to be sufficiently robust to describe the structure of the turbulent boundary layer relatively close to the wall (although there have been no direct observations of hairpins in the extremely high Reynolds numbers of the ASL to date). A consequence of this result is that while laboratory experiments at a lower Reynolds number may provide a reliable phenomenological picture of wall turbulence close to the wall, caution is required further from the wall ($z^+ \gg 10^3$) at high Reynolds numbers, e.g. when the edge of the boundary layer no longer confines the structural development. Our working hypothesis is that the region up to $z^+ = O(10^3)$, where scale interaction is observed to be particularly significant, is also the region where wall turbulence is well described by the hairpin paradigm in the ASL.

The present investigation does not provide an alternative model to the hairpin-packet paradigm, but rather complements it in a larger framework of interacting scales. The strong interactions between ramp-like structures and VLSMs in the wall region suggest indeed that those VLSMs may play a major role alongside the classical attached eddies not only in terms of momentum transfer but also in terms of mass, heat and vapour fluxes. A greater understanding of the formation and evolution of very-large-scale structures appears to be crucial for the understanding and the modelling of the high-Reynolds-number boundary layer.

The support of ONR grant N00014-08-1-0897 (programme manager Ron Joslin) is gratefully acknowledged.

REFERENCES

Acarlar, M. S. & Smith, C. R. 1987 A study of hairpin vortices in a laminar boundary layer. Part 2. Hairpin vortices generated by fluid injection. *J. Fluid Mech.* **175**, 43–83.

Adrian, R. J. 2007 Vortex organization in wall turbulence. *Phys. Fluids* **19**, 041301.

Adrian, R. J., Meinhart, C. D. & Tomkins, C. D. 2000 Vortex organization in the outer region of the turbulent boundary layer. *J. Fluid Mech.* **422**, 1–54.

del Álamo, J. C. & Jiménez 2003 Spectra of the very large anisotropic scales in turbulent channels. *Phys. Fluids* **15** (6), L41–44.

Balakumar, B. J. & Adrian, R. J. 2007 Large- and very-large-scale motions in channel and boundary layer flows. *Phil. Trans. R. Soc. Lond.* A **365**, 665–681.

Bandyopadhyay, P. R. & Hussain, A. K. M. F. 1984 The coupling between scales in shear flows. *Phys. Fluids* **27** (9), 2221–2228.

Christensen, K. T. & Adrian, R. J. 2001 Statistical evidence of hairpin vortex packets in wall turbulence. *J. Fluid Mech.* **431**, 433–443.

Chung, D. & McKeon, B. J. 2010 Large-eddy simulation investigation of large-scale structures in a long channel flow. *J. Fluid Mech.* (to appear).

Favre, A. J., Gaviglio, J. J. & Dumas, R. 1967 Structure of velocity space–time correlations in a boundary layer. *Phys. Fluids* **10**, S138–S145.

Flack, K. A., Schultz, M. P. & Shapiro, T. A. 2005 Experimental support for Townsend's Reynolds number similarity hypothesis on rough walls. *Phys. Fluids* **17** (3), 035102.

Ganapathisubramani, B., Longmire, E. & Marusic, I. 2003 Characteristics of vortex packets in turbulent boundary layers. *J. Fluid Mech.* **478**, 35–46.

Ganapathisubramani, B., Longmire, E. & Marusic, I. 2006 Experimental investigation of vortex properties in a turbulent boundary layer. *Phys. Fluids* **18**, 055105.

Guala, M., Hommema, S. E. & Adrian, R. J. 2006 Large-scale and very-large-scale motions in turbulent pipe flow. *J. Fluid Mech.* **554**, 521–542.

Guala, M., Metzger, M. & McKeon, B. J. 2010 Intermittency in the atmospheric surface layer: unresolved or slowly varying? *Physica* D **239** (14), 1251–1257.

Gulitski, G., Kholmyansky, M., Kinzelbach, W., Lüthi, B., Tsinober, A. & Yorish, S. 2007 Velocity and temperature derivatives in high-Reynolds-number turbulent flows in the atmospheric surface layer. Part 1. Facilities, methods and some general results. *J. Fluid Mech.* **589**, 57–81.

Hommema, S. E. & Adrian, R. J. 2003 Packet structure of surface eddies in the atmospheric boundary layer. *Boundary-Layer Met.* **106**, 147–170.

Hunt, J. & Morrison, J. 2000 Eddy structure in turbulent boundary layers. *Eur. J. Mech.* B *Fluids* **19** (5), 673–694.

Hutchins, N. & Marusic, I. 2007*a* Evidence of very long meandering features in the logarithmic region of turbulent boundary layers. *J. Fluid Mech.* **579**, 1–28.

Hutchins, N. & Marusic, I. 2007*b* Large-scale influences in near-wall turbulence. *Phil. Trans. R. Soc. Lond.* A **365**, 647–664.

Ikeda, T. & Durbin, P. 2007 Direct simulations of a rough-wall channel flow. *J. Fluid Mech.* **571**, 235–263.

Kim, K. C. & Adrian, R. J. 1999 Very large-scale motion in the outer layer. *Phys. Fluids* **11**, 417–422.

Kovasznay, L. S. G., Kibens, V. & Blackwelder, R. F. 1970 Large-scale motion in the intermittent region of a turbulent boundary layer. *J. Fluid Mech.* **41**, 283–325.

Krogstad, P. A., Kaspersen, J. H. & Rimestad, S. 1998 Convection velocities in a turbulent boundary layer. *Phys. Fluids* **18**, 055105.

Lee, M., Kim, J. & Moin, P. 1990 Structure of turbulence at high shear rate. *J. Fluid Mech.* **216**, 561–583.

LeHew, J., Guala, M. & McKeon, B. 2010 A study of convection velocities in a zero pressure gradient turbulent boundary layer. *Proc. 40th Fluid Dynamics Conference and Exhibit 28 June–1 July 2010*, Chicago, Illinois. AIAA Paper 2010-4474.

Mahrt, L. 1998 Stratified atmospheric boundary layers and breakdown of models. *Theor. Comp. Fluid Dyn.* **11**, 263–279.

Marusic, I. & Heuer, W. D. C. 2007 Reynolds number invariance of the structure inclination angle in wall turbulence. *Phys. Rev. Lett.* **99**, 114504.

Marusic, I. & Hutchins, N. 2008 Study of the log-layer structure in wall turbulence over a very large range of Reynolds number. *Flow Turbulence Combust.* **81** (1), 115–130.

Marusic, I., Mathis, R. & Hutchins, N. 2010 Predictive model for wall-bounded turbulent flow. *Science* **329**, 193–196.

Mathis, R., Hutchins, N. & Marusic, I. 2009 Large-scale amplitude modulation of the small-scale structures of turbulent boundary layers. *J. Fluid Mech.* **628**, 311–337.

McKeon, B. J. 2008 Scaling in wall turbulence: scale separation and interaction. *AIAA Paper* 2008-4237.

McKeon, B. J. & Sreenivasan, K. R. 2007 Scaling and structure in high Reynolds number wall-bounded flows. *Phil. Trans. R. Soc. Lond.* A **365**, 635–646.

Metzger, M. & Holmes, H. 2008 Time scales in the unstable atmospheric surface layer. *Boundary-Layer Meteorol.* **126**, 29–50.

Metzger, M., McKeon, B. J. & Holmes, H. 2007 The near-neutral atmospheric surface layer: turbulence and non-stationarity. *Phil. Trans. R. Soc. Lond.* A **365**, 859–876.

Metzger, M. M. & Klewicki, J. C. 2001 A comparative study of near-wall turbulence in high and low Reynolds number boundary layers. *Phys. Fluids* **13**, 692–701.

Monty, J. P., Stewart, J. A., Williams, R. C. & Chong, M. S. 2007 Large-scale features in turbulent pipe and channel flows. *J. Fluid Mech.* **589**, 147–156.

Morris, S. C., Stolpa, S. R., Slaboch, P. E. & Klewicki, J. 2007 Near-surface particle image velocimetry measurements in a transitionally rough-wall atmospheric boundary layer. *J. Fluid Mech.* **580**, 319–338.

Morrison, J. F. 2007 The interaction between inner and outer regions of turbulent wall-bounded flows. *Phil. Trans. R. Soc. Lond.* A **365**, 683–698.

Morrison, J. F., Jiang, W., McKeon, B. J. & Smits, A. J. 2004 Scaling of the streamwise velocity component in turbulent pipe flow. *J. Fluid Mech.* **508**, 99–131.

Morrison, W. R. B., Bullock, K. J. & Kronauer, R. E. 1971 Experimental evidence of waves in the sublayer. *J. Fluid Mech.* **47**, 639–656.

Orlandi, P. & Leonardi, S. 2008 Direct numerical simulation of three-dimensional turbulent rough channels: parameterization and flow physics. *J. Fluid Mech.* **606**, 399–415.

Perry, A. E. & Chong, M. S. 1982 On the mechanism of wall turbulence. *J. Fluid Mech.* **119**, 173–217.

Poggi, D., Porporato, A., Ridolfi, L., Albertson, J. & Katul, G. 2004 Interaction between large and small scales in the canopy sublayer. *Geophys. Res. Lett.* **31**, (5) L05102.

Theodorsen, T. 1952 Mechanism of turbulence. In *Proceedings of the 2nd Midwestern Conference on Fluid Mech.*, pp. 1–19. Ohio State University, Columbus, Ohio.

Tomkins, C. D. & Adrian, R. J. 2003 Spanwise structure and scale growth in turbulent boundary layers. *J. Fluid Mech.* **490**, 37–74.

Tutkun, M., George, W. K., Delville, J., Stanislas, M., Johansson, P. B. V., Foucaut, J. M. & Coudert, S. 2009 Two-point correlations in high Reynolds number flat plate turbulent boundary layers. *J. Turbulence* **10** (21), 1–22.

Waleffe, F. 2001 Exact coherent structures in channel flow. *J. Fluid Mech.* **435**, 93–102.

Wu, X. & Moin, P. 2009 Direct numerical simulation of turbulence in a nominally zero-pressure-gradient flat-plate boundary layer. *J. Fluid Mech.* **630**, 5–41.

Zhou, J., Adrian, R. J. & Balachandar, S. 1996 Autogeneration of near wall vortical structure in channel flow. *Phys. Fluids* **8**, 288–291.

Zhou, J., Adrian, R. J., Balachandar, S. & Kendall, T. M. 1999 Mechanisms for generating coherent packets of hairpin vortices in channel flow. *J. Fluid Mech.* **387**, 353–396.